We are IntechOpen, the world's leading publisher of Open Access books
Built by scientists, for scientists

6,900
Open access books available

186,000
International authors and editors

200M
Downloads

Our authors are among the

154
Countries delivered to

TOP 1%
most cited scientists

12.2%
Contributors from top 500 universities

CLARIVATE ANALYTICS
BOOK CITATION INDEX
INDEXED

WEB OF SCIENCE™

Selection of our books indexed in the Book Citation Index
in Web of Science™ Core Collection (BKCI)

Interested in publishing with us?
Contact book.department@intechopen.com

Numbers displayed above are based on latest data collected.
For more information visit www.intechopen.com

Chapter

Driving Control Technologies of New High-Efficient Motors

Chang-Ming Liaw, Jia-Hsiang Zhuang, Shih-Wei Su,
Kai-Wei Hu and G. Vijay Kumar

Abstract

Although induction motor is the most commonly used actuator in the industry, its efficiencies are difficult to upgrade due to the existence of rotor copper losses. Permanent-magnet synchronous motor (PMSM) and synchronous reluctance motor (SynRM) are the two new motors being able to achieve the IE4-class and even the IE5-class efficiency. As to the switched reluctance motor (SRM), it lacks commercialized motors and power modules being available. For establishing high-performance PMSM and SynRM drives, many key affairs must be properly treated, which are introduced in this article. The contents presented in this chapter include: (1) interdisciplinary affairs of motor drives, (2) comparative characteristics and applications of commonly used motors, (3) reversible and generator operations for specific motors, (4) power electronic converters for motor drives, (5) possible new high-efficient motor drives, (6) PMSM drives, (7) SynRM drives, (8) some key issues of PMSM drives, (9) some key issues of SynRM drives, (10) example of PMSM drive, and (11) example of SynRM drive.

Keywords: PMSM, SynRM, dynamic modeling, commutation, current control, speed control, efficiency

1. Introduction

Induction motors [1–3] are still the most popularly applied motor owing to their simple structures, ease of operation, and mature driving technologies. However, their best efficiencies are generally still in IE3-class due to the existence of rotor copper losses. Upgrading the efficiencies of IMs to IE4-class via using high-grade core and rotor cage materials will not be cost-effective. Permanent-magnet synchronous motor (PMSM) and synchronous reluctance motor (SynRM) [2–6] are the two new motors being able to achieve the IE4-class and even the IE5-class efficiency. As to the switched reluctance motor (SRM) [7], although it may also possess the potential, it still lacks commercialized motors and power modules being available.

To establish a high-performance PMSM drive, the proper match between the available source, the interface converter, the motor drive, and the mechanical load must be made. Some major affairs to be properly treated include: (i) physical modeling and parameter estimation [8, 9]; (ii) current control [10–13]: generally, the current control methods can be categorized into hysteresis controls, ramp-comparison controls and predictive controls; (iii) speed control [14–17]; (iv) direct torque control based on space-vector PWM [18]; (v) commutation shift and

field-weakening control [19–25]: through appropriate d-axis field current setting or commutation shift, the developed torque can be increased by utilizing the reluctance torque component effectively. In the case of constant power, it can extend the speed range through field-weakening; (vi) voltage boosting [26–28]: for a battery-powered EV PMSM drive, the equipped battery followed interface DC/DC converter providing adjustable DC-link voltage can increase the battery voltage selection flexibility and the overall drive system rating utilization. The buck-boost bidirectional interface converters are adopted in the PMSM motor drive [27]. It can step down the voltage from battery; hence the lower DC-link voltage under lower speed can improve the efficiency. As the motor drive is drawn from the mains, the single-phase or three-phase switch-mode rectifiers (SMRs) [29–32] must be equipped to achieve the DC-link voltage boosting task.

For a standard PMSM drive, the rotor absolute position is necessary to make its vector control. However, for avoiding the risk of sensor failure, the position sensorless controlled motor drive is preferable. Generally, the existing PMSM position sensorless control approaches can be classified into [33–35]: (i) methods based on the measured and/or identified machine parameters [36, 37]; (ii) methods based on rotor saliency and magnet anisotropy: the high-frequency injection approaches are the typical ones. The high-frequency sinusoidal-wave [38–40] or square-wave [41, 42] voltage with suited amplitude and frequency is injected into the studied motor, and the detected current is processed to yield the observed rotor position. These approaches can be successfully operated under low speed including standstill, and no machine parameters are needed. However, the injected signal will yield high-frequency noise, lower efficiency and the back-EMF harmonics in IPMSM may cause the estimated rotor position error; (iii) observer based methods [36, 43, 44]: these include adaptive observers, sliding mode observers, Kalman filter observers and reduced-order observers, etc.; (iv) back-EMF methods [45–47]: these methods are obviously not suitable for EV due to its frequent accelerating/decelerating operations; and (v) hybrid methods [48, 49].

As generally recognized, PMSM possesses high power density and efficiency. However, its manufacture process is complicated with higher cost. And it has the demagnetization risk. As to the synchronous reluctance motor (SynRM), although it has no permanent magnet torque component, good performance/cost-compromised performance can still be obtained if the proper switching control is made. It possesses high application potential, especially for high-speed driving, since its rotor is rigid and cogging torque free from having no permanent magnets and conductors.

Since only some air slots are existed in the rotor of a SynRM, its energy conversion characteristics are significantly affected by rotor geometry [50–52]. The rotor is assembled with stacked silicon steels, which leads the rotor to be easily saturated, and the iron loss is comparatively higher than PMSM. Hence, considering iron loss and magnetic saturation is necessary for achieving high performance and efficiency.

In efficiency optimization of a SynRM, both the copper loss and the iron loss must be considered. The copper loss is load-dependent, while the iron loss is related to the air-gap flux level. Basically, loss minimization approaches [53–62] for SynRM can be roughly categorized into loss model-based control and searching control. The former approaches minimize the power consumption by setting the optimal d-axis current command, which is derived from the loss function using machine parameters. Obviously, the resulted control performance is affected by the motor parameter variations, especially the d-axis inductance. As to the searching methods, their performances are insensitive to motor parameter variations. However, the complicated searching process usually causes the sluggish dynamic response, torque ripple, and additional losses. Finally, for illustrating the key technological affairs introduced in this article, the example battery/supercapacitor powered EV PMSM drive [63] and SMR-fed SynRM drive [64, 65] are presented in Section 5 and Section 6.

2. Basic motor drive system configuration

As shown in **Figure 1**, motor drive is an interdisciplinary mechatronic system including motor, mechanical load, power converter, control scheme, transducing, and sensing schemes. The proper design of motor and the proper match between system-constituted components should be made for yielding good driving performance.
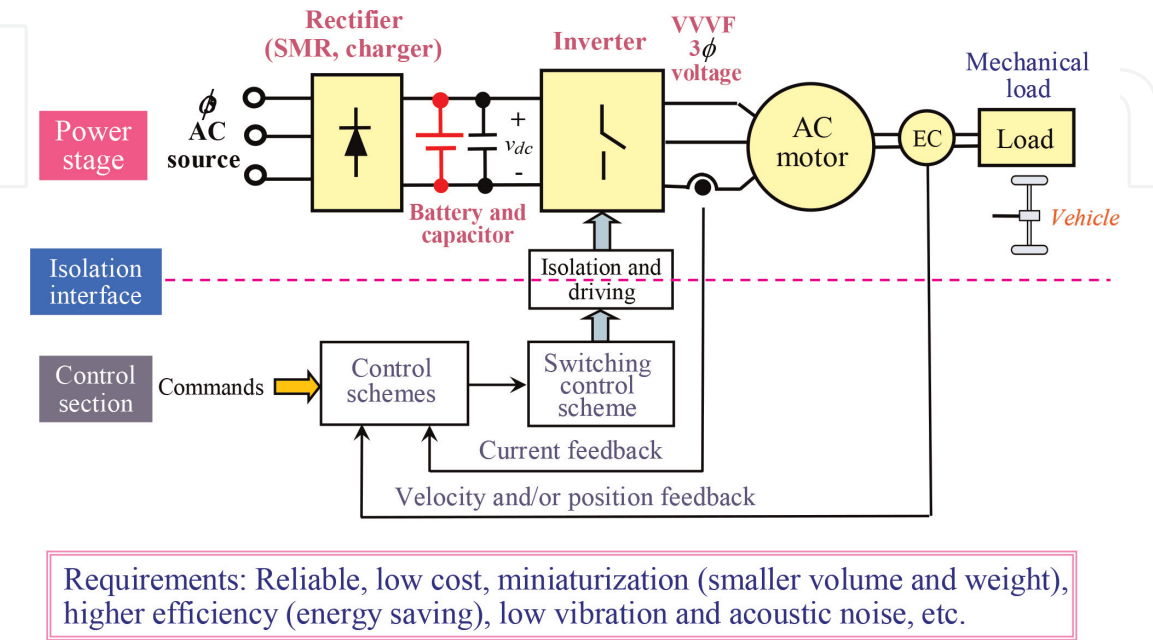
Figure 1.
Typical motor drive system configuration.
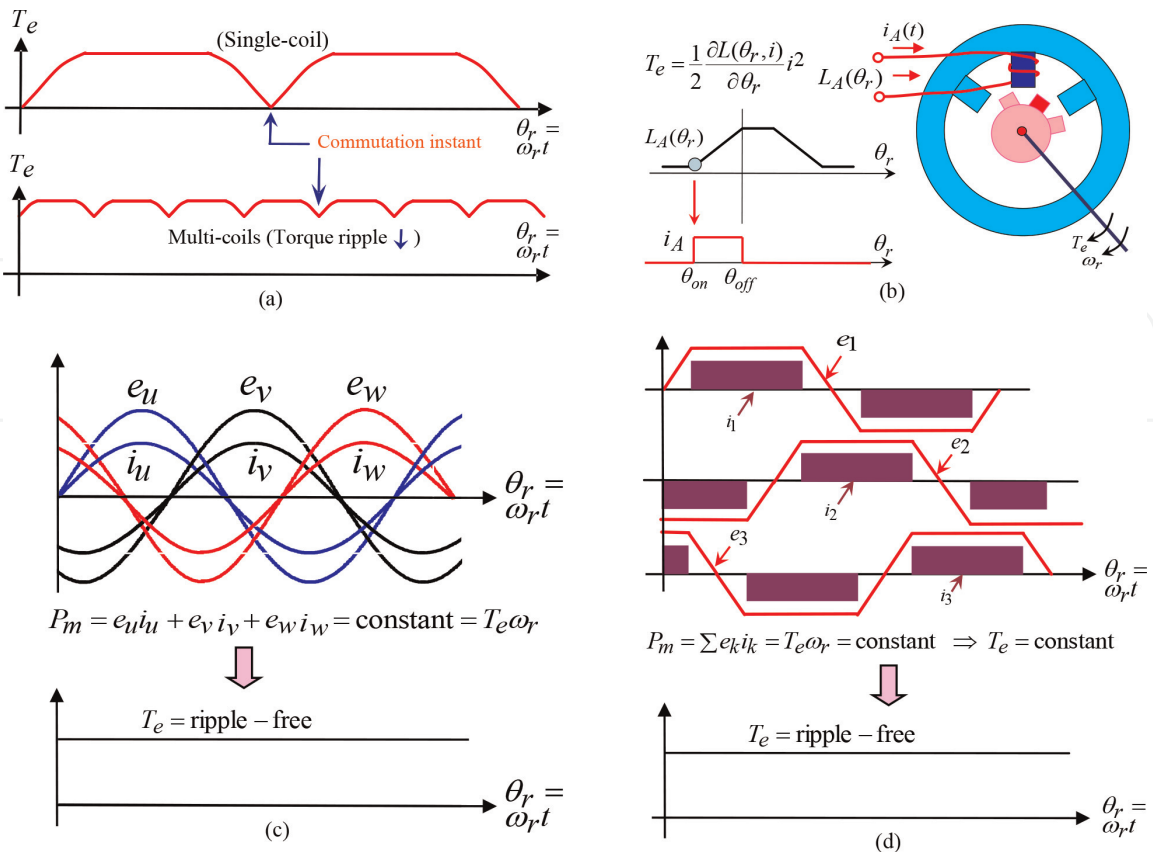
Figure 2.
Sketched ideal developed torque characteristics of some motors: (a) DCM, (b) SRM, (c) three-phase sine-wave PMSM (d) three-phase square-wave PMSM.

The commonly used motors include brushed DC motor (DCM), induction motor (IM), and synchronous motor (SM) consisting of permanent-magnet synchronous motor (PMSM), synchronous reluctance motor (SynRM), switched reluctance motor (SRM), etc. The ideal developed torque characteristics of some typical motors are sketched in **Figure 2**. In reality, each type of motor possesses its distinct affairs, which must be properly treated.

3. Permanent-magnet synchronous motors
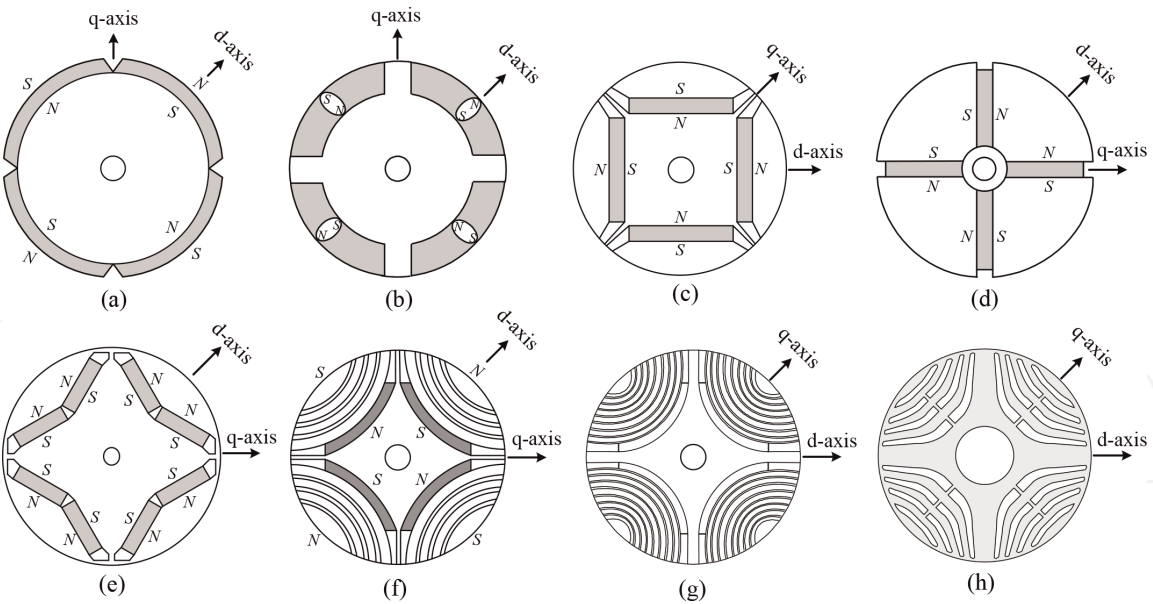
3.1 Structural features of synchronous motors

Except for the slot-less stator, the slotted and salient-pole stators are shown in **Figure 3a** and **b**. The former is mainly employed for forming distributed armature winding with sinusoidal currents. It is suitable for low-speed driving applications because it generates smoother developed torque. The salient-pole stator in **Figure 3b** is used for concentrated windings. This winding has higher efficiency owing to its lower copper losses. However, it possesses higher torque ripple and thus only suited for speed driving applications.

Some rotor structures of SM are sketched in **Figure 4a**–**g**. The SPMSM shown in **Figure 4a** possesses less cogging torque and smoother developed torque. Hence, it is suitable for low-speed driving applications. In order to increase the rigidity, one can adopt the inset SPMSM shown in **Figure 4b**. There are many types of interior PMSM (IPMSM) with various shapes of PM. The two typical rotor structures of IPMSM with buried and interior magnets are shown in **Figure 4c** and **d**. The existence of saliency allows them to produce reluctance torque in addition to electromagnetic torque. And the field weakening is simpler to achieve. For higher speed driving applications, one can adopt the permanent-magnet-assisted SynRM (PMa-SynRM) shown in **Figure 4e**. Two types of SynRM rotor structure are shown in **Figure 4f** and **g**, namely, the axially laminated anisotropy (ALA) rotor and the transversally laminated anisotropy (TLA) rotor.

Comments: SynRM belongs to SM having: (i) distributed armature windings; and (ii) PM-free rotor with air slots. As to the switched reluctance motor (SRM), its features lie in: (i) concentrated armature windings and (ii) teethed rotor. It follows that these two reluctance machines have the major comparative features: (i) they all have only reluctance torque, and the developed torque or power is highly affected

(a)   (b)
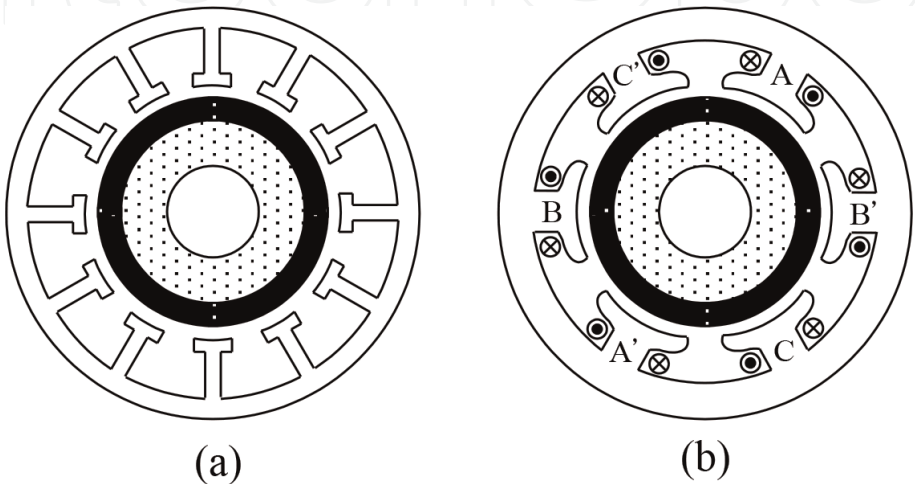
Figure 3.
Typical stator structures of synchronous motors: (a) slotted and (b) salient-pole.

Figure 4.
Some typical rotor structures of synchronous motors: (a) SPMSM, (b) inset SPMSM, (c) radial IPMSM, (d) tangential IPMSM, (e) hybrid V-shape IPMSM, (f) PMASynRM, (g) ALA SynRM, and (h) TLA SynRM.

by commutation instant setting and (ii) although they all possess high ripple torques under low speed, the one yielded by SynRM is less owing to distributed armature with sinusoidal current excitation.

3.2 Physical modeling of PMSM

3.2.1 Voltage equations

Figure 5 shows the configuration of a Y-connected three-phase 2-pole PMSM. The Y-connected resistors across the armature terminals are used to estimate the motor phase back-EMF under no-load, that is, $v_{an'} \approx e_{as}$. The following assumptions are made for making analytic derivation: (i) symmetrical and sinusoidally distributed three-phase armature windings, (ii) sinusoidal armature back-EMFs, and (iii) linear magnet circuit. And the rotor position θ_r is defined as the angle between as-axis and the sensed q-axis.

The phase (a-phase as an example, the ones for the other two phases, can be written analogously) voltage equation can be expressed as:
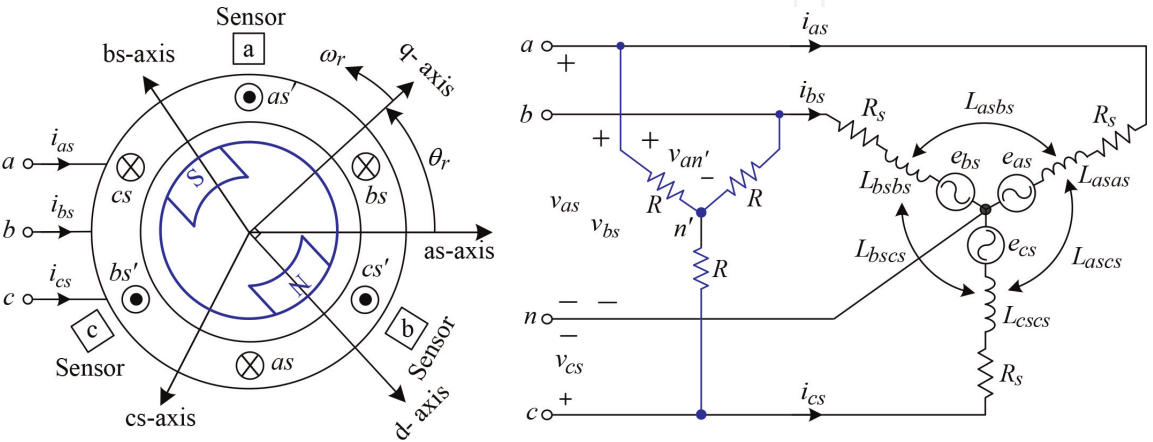
Figure 5.
Configuration of an elementary three-phase two-pole Y-connected PMSM.

$$v_{as} = R_s i_{as} + \frac{d}{dt}\lambda_{as} = R_s i_{as} + \frac{d}{dt}(L_{asas}i_{as} + L_{asbs}i_{bs} + L_{ascs}i_{cs}) + e_{as} \qquad (1)$$

$$L_{asas} = L_{ls} + L_A + L_B \cos 2\theta_r \qquad (2)$$

$$e_{as} = \lambda_m^{'r}\omega_r \cos\theta_r \underline{\Delta} \hat{E}_{as}\cos\theta_r \qquad (3)$$

$$\theta_r = \theta_r(0) + \int_0^t \omega_r(\zeta)d\zeta \qquad (4)$$

where v_{as} is winding terminal voltages, i_{as} is winding current, R_s is winding resistance, λ_{as} is winding flux linkage, $\lambda_m^{'r}$ is peak flux linkage contributed by the rotor permanent magnet, L_{asas} is winding self-inductance, L_{asbs} is mutual inductance, L_{ls} is winding leakage inductance, θ_r is rotor electrical angular position, $\theta_r(0)$ is the initial position of q-axis relative to a-axis, ω_r is rotor electrical angular speed, e_{as} is back electromotive force (EMF), and $\hat{E}_{as}$ is the peak value of e_{as}.

By applying rotor rotating frame transformation, the voltage equations in dq-frame can be written as:

$$v_{qs} = \left(R_s + pL_q\right)i_{qs} + \omega_r L_d i_{ds} + \omega_r \lambda_m^{'r} \qquad (5)$$

$$v_{ds} = \left(R_s + pL_d\right)i_{ds} - \omega_r L_q i_{qs} \qquad (6)$$

$$L_q = L_{ls} + L_{mq} = L_{ls} + \frac{3}{2}(L_A + L_B) \qquad (7)$$

$$L_d = L_{ls} + L_{md} = L_{ls} + \frac{3}{2}(L_A - L_B) \qquad (8)$$

where $L_q(L_d)$ denotes q-axis (d-axis) inductance and $L_q > L_d$.

3.2.2 Torque and mechanical equations

The electromagnetic developed torque and mechanical equations of a PMSM drive in dq-frame can be expressed as:

$$T_e = \frac{3P}{4}\left[\lambda_m^{'r}i_{qs} + (L_d - L_q)i_{qs}i_{ds}\right] = \frac{3P}{4}\left[\lambda_m^{'r}\hat{I}_{as}\cos\beta + \frac{L_d - L_q}{2}\hat{I}_{as}^2\sin 2\beta\right] = T_L + B\omega_r + J\frac{d\omega_r}{dt}$$

$$(9)$$

where P is pole number, $\hat{I}_{as}$ is peak of a-phase current, the variables β denotes the shift angle between q-axis and peak of a-phase current, T_L is load torque, B is total damping coefficient, and J is total inertia constant.

3.3 Measurement of motor key parameters

Before establishing the motor drive, some key motor parameters must be measured to comprehend the characteristics of the studied motor. **Figure 6** shows the experimental mechanism for conducting the measurements.

3.3.1 Winding resistance and inductances

For the Y-connected PMSM with isolated neutral as indicated in **Figures 5** and **6**, from Eq. (1), the inductance and resistance of PMSM between a-phase and b-phase can be expressed as:

PMSM
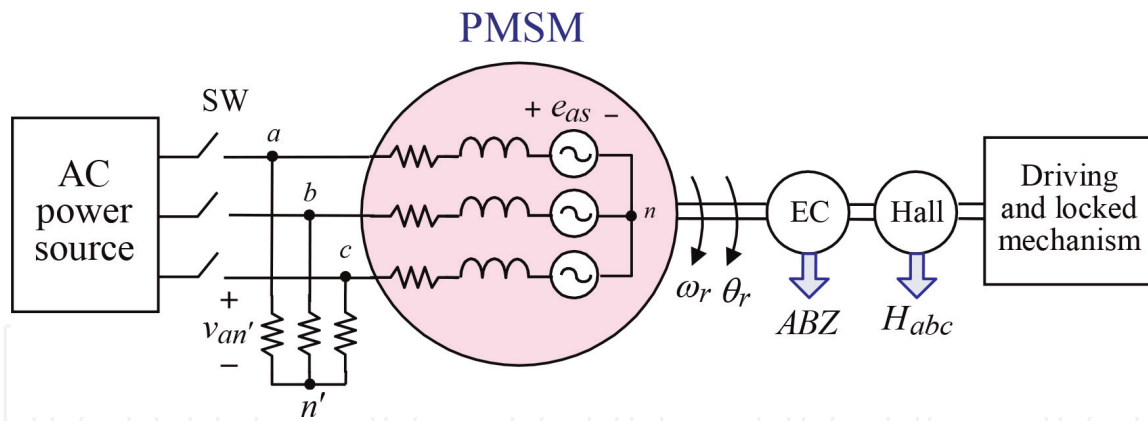
Figure 6.
Parameter measurement mechanism for SMs.

$$R_{ab} = 2R_s, \quad L_{ab}(\theta_r) = 2L_{ls} + 3L_A - 3L_B \cos\left(2\theta_r - \frac{2\pi}{3}\right) \tag{10}$$

And the q-axis and d-axis inductances of Eqs. (7) and (8) can be expressed from Eq. (10) as:

$$L_q = \frac{L_{asbs,\,max}}{2} = \frac{1}{2}L_{asbs}\left(\theta_r = -\frac{\pi}{6}\right) = L_{ls} + \frac{3}{2}L_A + \frac{3}{2}L_B \tag{11}$$

$$L_d = \frac{L_{asbs,\,min}}{2} = \frac{1}{2}L_{asbs}\left(\theta_r = \frac{\pi}{3}\right) = L_{ls} + \frac{3}{2}L_A - \frac{3}{2}L_B \tag{12}$$

A. *Winding resistance*: the armature winding resistance $R_s = R_{ab}/2$ can be estimated by DC excitation method.

B. *Winding inductances*: the $L_{ab}(\theta_r)$ can be measured using the LCR meter under various frequencies at different rotor positions. Then the q-axis and d-axis inductances L_q and L_d can be obtained from Eqs. (11) and (12). However, the inductance-saturated effects cannot be acquired for the small-signal excitation. On the other hand, one can apply the step-response method under various current levels.

3.3.2 Back-EMF and PM flux linkage λ_m'

As shown in **Figure 5**, three Y-connected resistors with a reasonably high resistance ($R = 100\,k\Omega$) are connected at the stator terminals to observe the motor phase back-EMF under no-load. By letting $i_{as} = i_{bs} = i_{cs} = 0$, the back-EMF can be found from Eqs. (1) and (3) as:

$$e_{as} = \hat{E}_{as} \cos\theta_r = v_{as}\big|_{NL} \approx v_{an'}\big|_{NL} \tag{13}$$

And $\lambda_m^{'r}$ can be obtained from Eq. (3) as:

$$\lambda_m^{'r} = \frac{\hat{E}_{as}}{P/2 \times \omega_r}\,(\text{Wb}) \tag{14}$$

3.3.2.1 Measured examples

A. **Figure 7a** and **b** depict the measured back-EMFs and their spectra of two examples of PMSMs: (a) under 1000 rpm of a three-phase SPMSM, 5 kW,

24.5 N-m, 8-pole, 2000 rpm and (b) under 1000 rpm of a three-phase IPMSM, 1 kW, 3.23 N-m, 6-pole, 3000 rpm.

B. *Observations*: for the IPMSM, the distorted back-EMF waveform with eleventh and thirteenth orders are observed. The influences of back-EMF harmonics on the current control and the high-frequency-injected position sensorless control must be considered.

3.4 Some key issues

Figure 8 shows some key issues affecting the performance of PMSM and SynRM drives. The typical ones include: (i) suitable motor type selection, (ii) motor parameters and dynamic model estimation, (iii) commutation instant setting and shifting, (iv) inverter and its PWM switching control, (v) field weakening, (vi) DC-link voltage boosting, (vii) regenerative braking operation, (viii) generator operation, and (ix) position sensorless control. Some comments are given below:

A. Motor selection: the stator and rotor structural features of some SMs have been explored in Section 3.1. The comparative loss and efficiency characteristics of some PMSMs and SynRM are depicted in **Figure 9** [2, 3]. Basically, as the speed is increased, the PMSM with fewer permanent magnets is chosen for the ease of conducting field-weakening control. And finally, the SynRM or SRM is employed for higher speed driving applications.

B. Commutation: from Eqs. (3)–(9), one can be aware that the back-EMF and the developed torque of PMSM are highly affected by the speed, load, and commutation angle. The commutation shifting angle β must be properly set and tuned to yield better developed torque. Commutation-advanced shift possesses field-weakening effects to reduce the back-EMF effects on the winding current response. It is worth noting that the commutation shift can
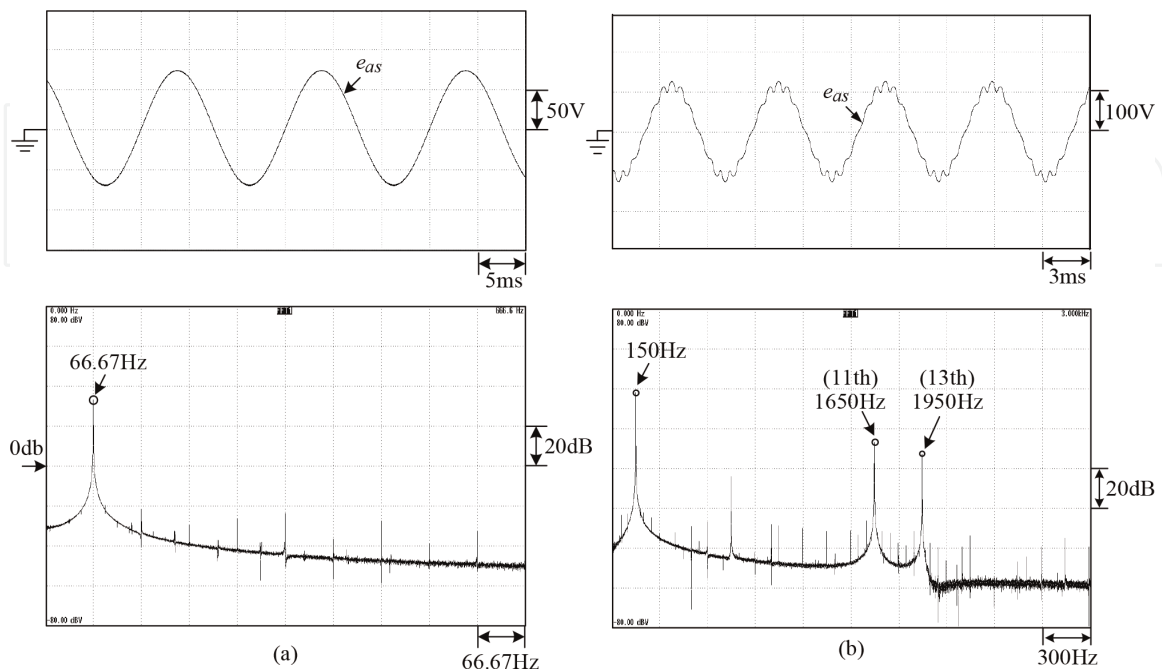
Figure 7.
Measured back-EMFs and their spectra of two examples of PMSMs: (a) under 1000 rpm of a three-phase SPMSM, 5 kW, 24.5 N m, 8-pole, 2000 rpm and (b) under 1000 rpm of a three-phase IPMSM, 1 kW, 3.23 N m, 6-pole, 3000 rpm.
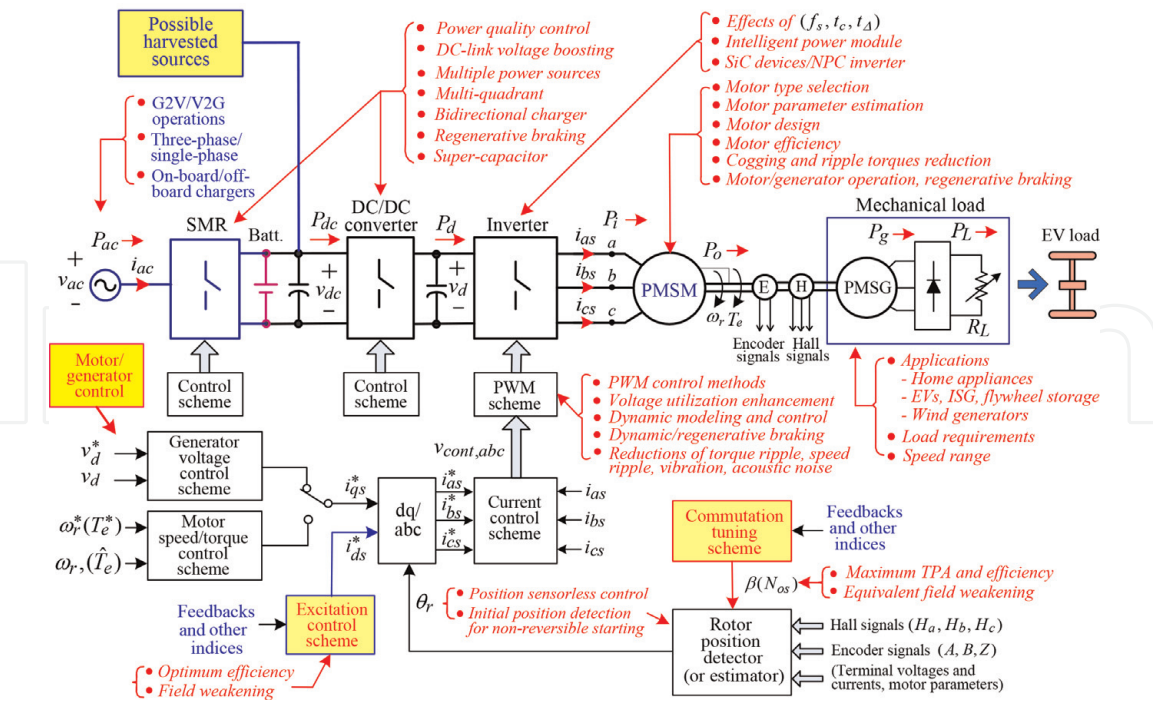
Figure 8.
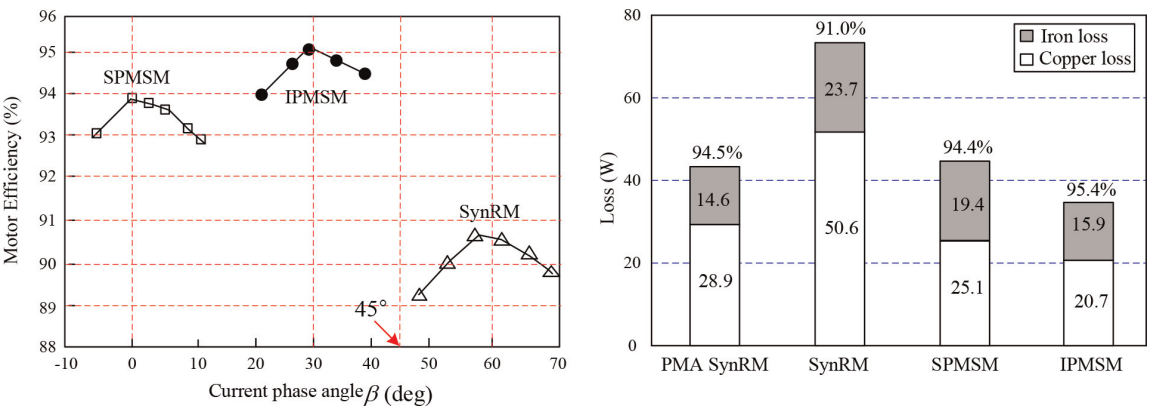*Some key issues of PMSM and SynRM drives.*

Figure 9.
Comparative efficiencies of some typical synchronous motors.

also be equivalently achieved via directly setting the d-axis field current command. Basically, the commutation advanced shifting angles for various SMs are (i) SPMSM, $\beta = 0°$; (ii) SynRM, $\beta = 45°$ theoretically; and (iii) IPMSM and PMASynRM, $\beta = 0 \sim 45°$. This fact can also be observed from **Figure 9**.

C. Current control and effects of current ripple: for an inverter-fed AC motor drive, its driving characteristics are greatly affected by the adopted PWM approach, including fundamental frequency control and harmonic spectral features. The current-controlled PWM (CCPWM) scheme is normally applied for high-performance motor drive. As indicated in **Figure 10a** and **b**, the CCPWM scheme can be realized in abc-domain or dq-domain.

D. In some special application cases, the SPMSM is still adopted as the actuator for very high-speed driving applications with very compact volume. In these cases, the accurate commutation instant setting is very critical for avoiding

magnet demagnetization, especially for position sensorless controlled drive. Moreover, the suited filtering chokes must be inserted between the inverter and the motor, as indicated in **Figure 11**.

E. Voltage boosting: under high speed, the sufficiently high back-EMF may make the winding current tracking performance sluggish as indicated in **Figure 11** and thus yield the worsened developed torque. Voltage boosting is the effective means [26–28] to solve these problems. To accomplish this goal, one must equip the suited SMR or DC-DC interface converter for the motor drive being powered from the three-phase/single-phase mains or the battery. Some typical schematic arrangements of the bilateral SMRs and DC-DC interface converters are shown in **Figures 12** and **13**.
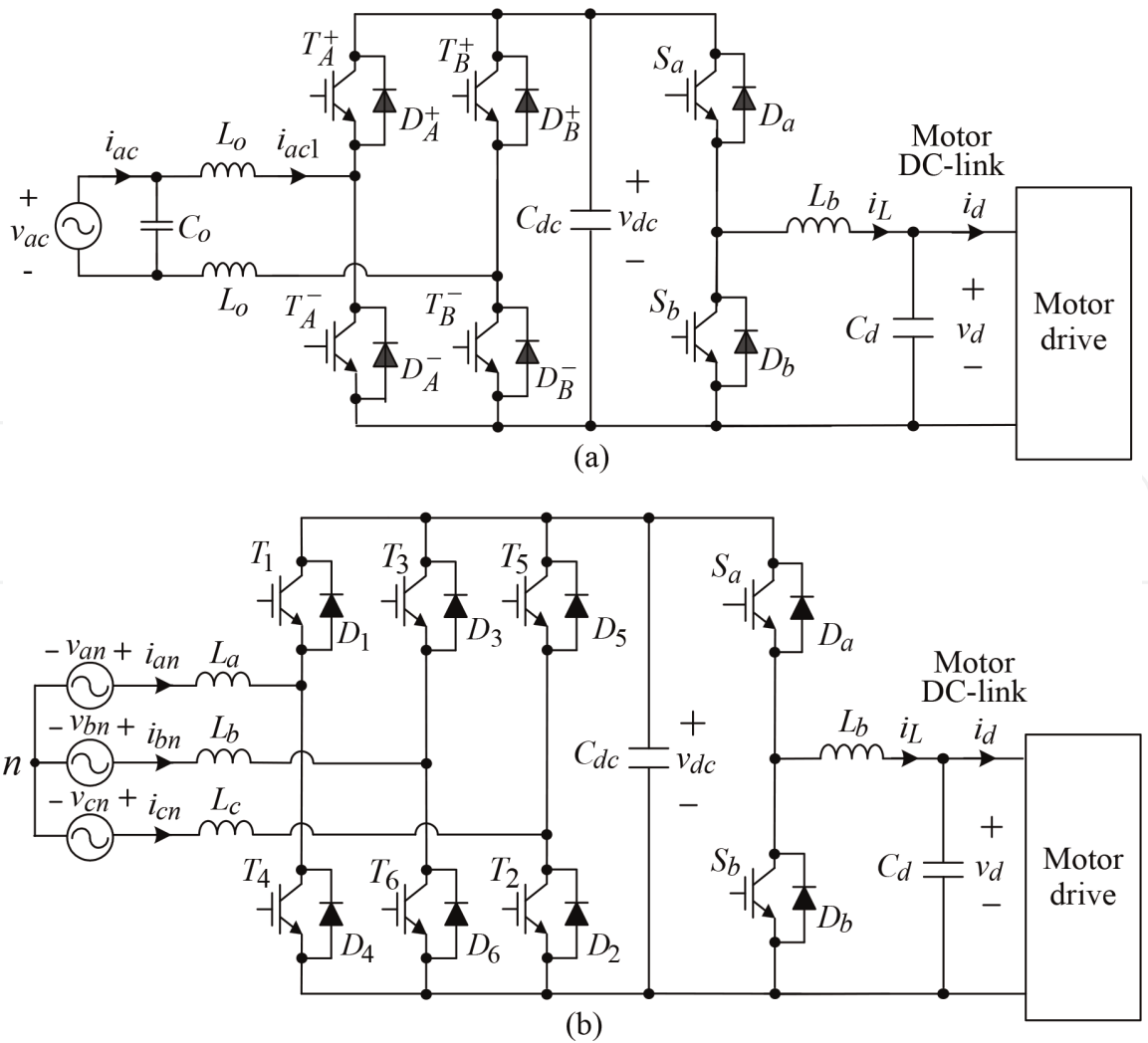

(a)

(b)
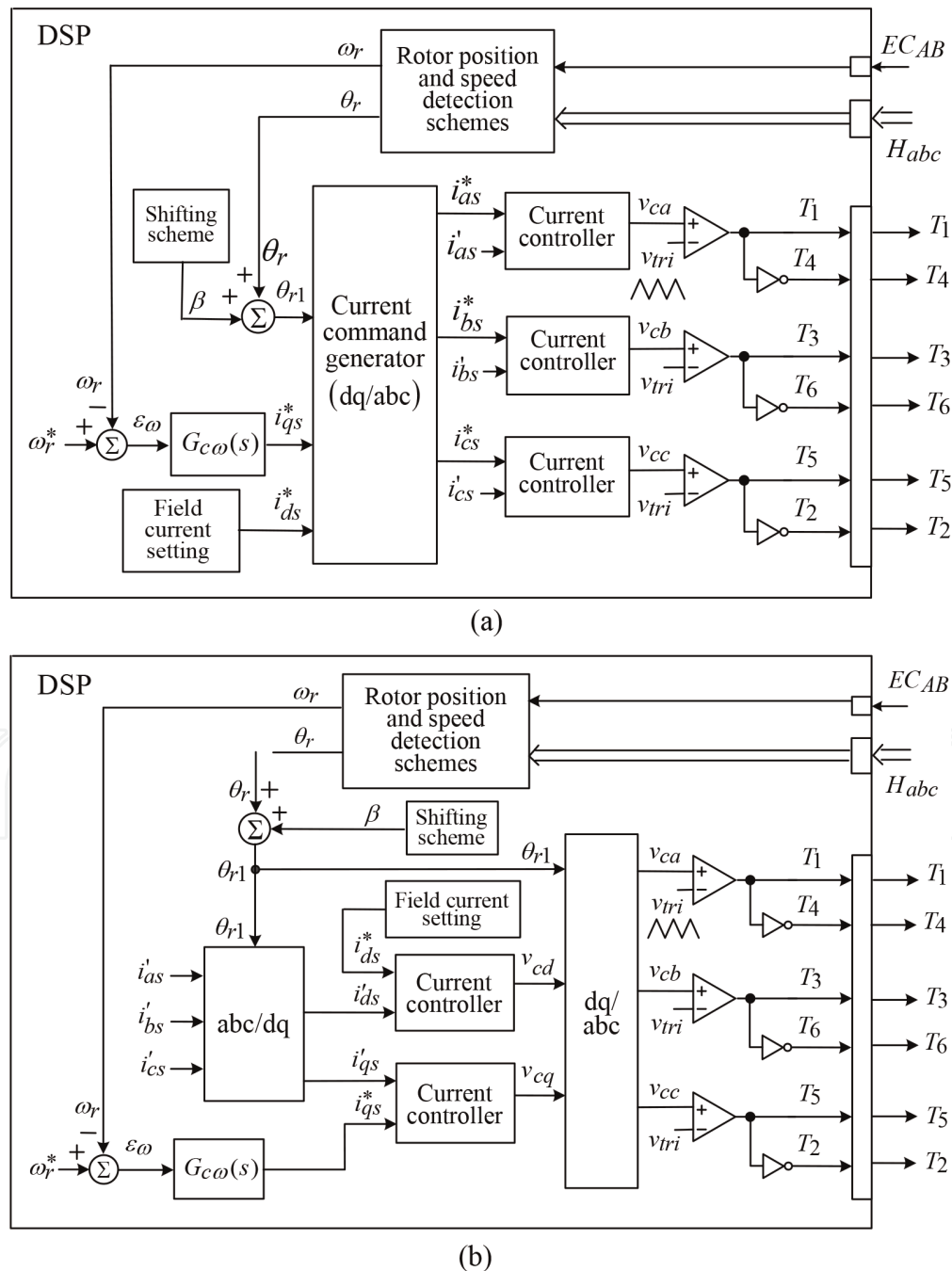
Figure 10.
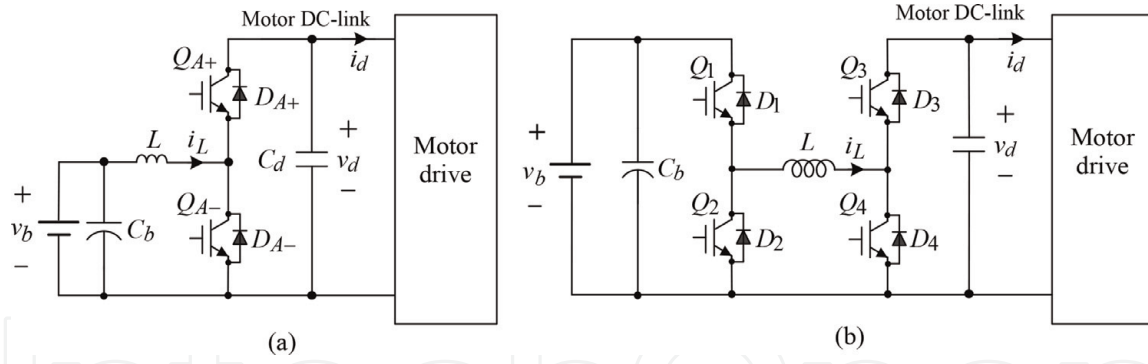*Configurations of CCPWM schemes in (a) abc-domain and (b) dq-domain.*

Effects of non-ideal current waveforms
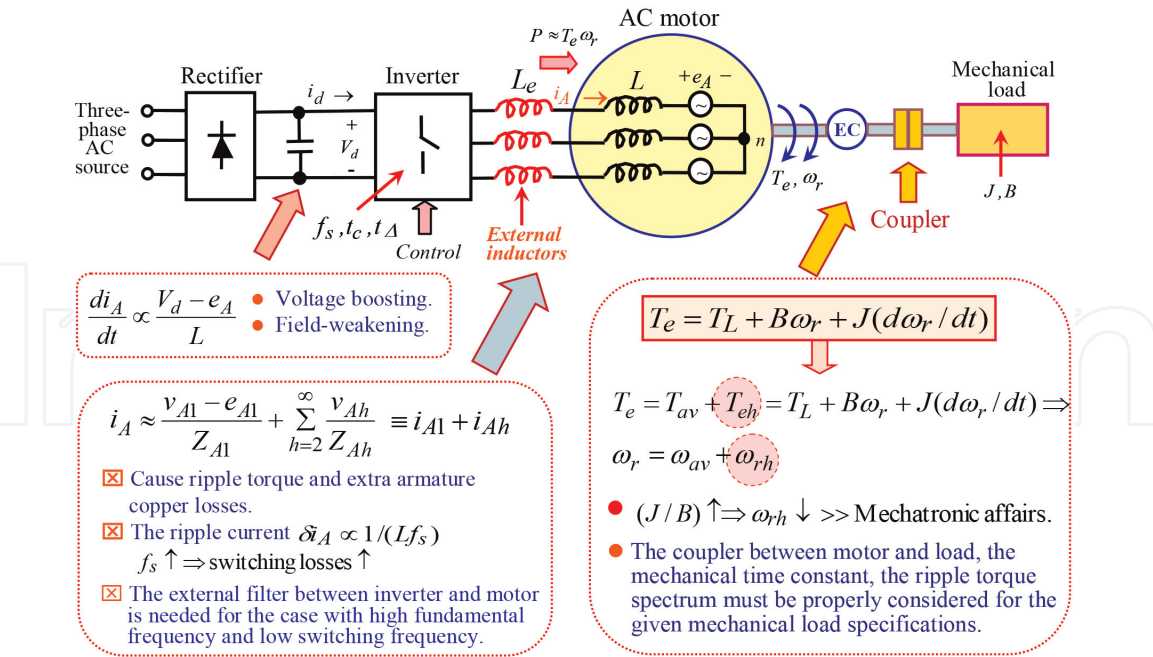
Figure 11.
Effects of DC-link voltage level and non-ideal winding current waveforms on the AC motor drive driving characteristics.

(a)

(b)

Figure 12.
Motor drive with bidirectional SMR front end: (a) three-phase SMR and (b) single-phase SMR.

Figure 13.
Motor drive with bidirectional DC-DC converter front end: (a) one-leg boost-buck converter and (b) H-bridge converter.

F. Generator operation of PMSM: according to Eq. (9), the generating mode of a PMSM is achieved as: PMSG: Q-axis torque current command is directly set to be negative; Regenerative braking and reversible operation of PMSM: the q-axis torque current is automatically set to be negative by the control scheme to achieve normal operations.

G. Sensorless control: basically, the most commonly used position sensorless methods are the observer back-EMF based and the HFI approaches. The former methods can only possess satisfactory running characteristics above a certain speed. Moreover, the motor must be started under traditional synchronous motor mode. By contrast, the HFI approach can be operated effectively in standstill and low speed, so this approach is applicable to frequent-starting occasions, for example, electric vehicles, tractions, elevators, etc. No motor parameters and externally added schematics are needed in constructing a HFI sensorless controlled SynRM drive. However, as mentioned above, the injected signal will yield acoustic noise and lower efficiency, and the back-EMF harmonics of IPMSM and SynRM may cause the estimated rotor position error.

4. Synchronous reluctance motors

4.1 Structural features

As shown in **Figures 3** and **4**, SynRM possesses distributed armature windings and PM-free rotor with air slots. The armature is exited with sinusoidal currents. Since it has only the reluctance torque, the developed torque is highly affected by commutation instant setting.

4.2 Physical modeling

4.2.1 Neglecting core loss

Different from the PMSM shown in **Figure 5**, the d-axis is conventionally chosen as the reference as indicated in **Figure 14a**. Following the similar deriving procedure described in the previous section, one can yield the voltage equations of SynRM:

$$v_{qs} = \left(R_s + L_q \frac{d}{dt}\right)i_{qs} + \omega_r L_d i_{ds}, \, v_{ds} = \left(R_s + L_d \frac{d}{dt}\right)i_{ds} - \omega_r L_q i_{qs} \tag{15}$$
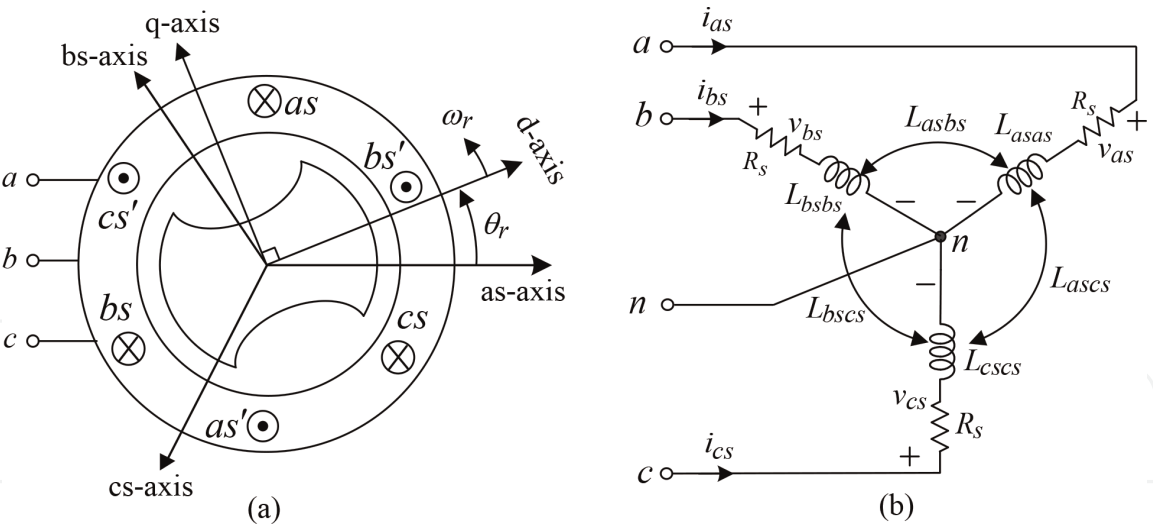
Figure 14.
A two-pole three-phase synchronous reluctance motor: (a) configuration and (b) Y-connected armature circuit.

$$L_q = L_{ls} + L_{mq} = L_{ls} + \frac{3}{2}(L_A - L_B), L_d = L_{ls} + L_{md} = L_{ls} + \frac{3}{2}(L_A + L_B) \qquad (16)$$

with L_{mq} (L_{md}) being the q-axis (d-axis) magnetizing inductances, respectively. Obviously, $L_d > L_q$ can be observed from Eq. (16).

The developed torque and mechanical equations of a SynRM drive are:

$$T_e = \frac{3P}{4}(L_d - L_q)i_{qs}i_{ds} = \frac{3P}{4}\frac{L_d - L_q}{2}\hat{I}_{as}^2 \sin 2\beta = T_L + B\omega_r + J\frac{d\omega_r}{dt} \qquad (17)$$

where $\hat{I}_{as}$ is peak of a-phase current, the variable β denotes the shift angle between the d-axis and the peak of a-phase current, $i_{qs} = \hat{I}_{as} \sin \beta$ and $i_{ds} = \hat{I}_{as} \cos \beta$.

Comments: from Eq. (17) one can find some facts: (i) it only possesses the reluctance torque, which is nonlinear and (ii) although $\beta = 45°$ can be set to yield the maximum torque, theoretically, the proper setting of β is required for maximizing T_e in reality.

4.2.2 Considering core loss

For a SynRM, the core loss is more significant than other motors. The d-axis and q-axis equivalent circuits considering iron loss with R_c are shown in **Figure 15a**. And **Figure 15b** shows the phasors of torque currents and terminal currents considering iron loss. From which, the terminal currents i_{qs} and i_{ds} can be expressed using the torque currents i_{mq} and i_{md} as:

$$\begin{bmatrix} i_{qs} \\ i_{ds} \end{bmatrix} = \frac{L_d L_q}{R_c}\begin{bmatrix} (s + R_c/L_q)/L_d & \omega_e/L_q \\ -\omega_e/L_d & (s + R_c/L_d)/L_q \end{bmatrix}\begin{bmatrix} i_{mq} \\ i_{md} \end{bmatrix} \qquad (18)$$
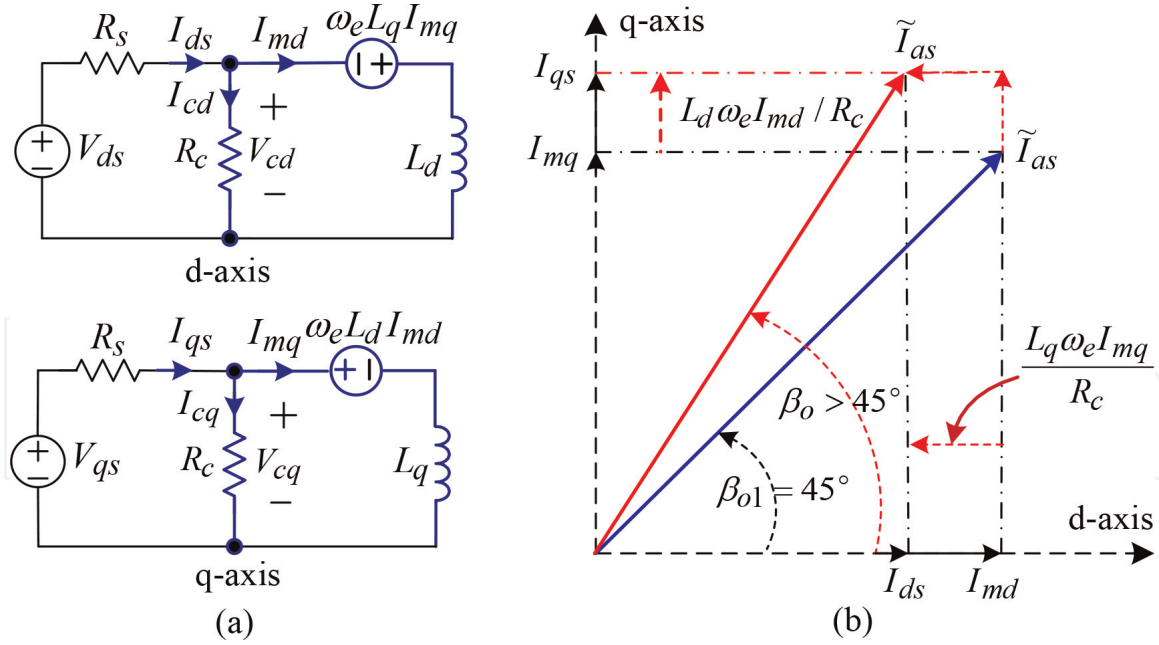
And the steady-state expressions of Eq. (4) are:

$$\begin{bmatrix} I_{qs} \\ I_{ds} \end{bmatrix} = \begin{bmatrix} 1 & L_d\omega_e/R_c \\ -L_q\omega_e/R_c & 1 \end{bmatrix}\begin{bmatrix} I_{mq} \\ I_{md} \end{bmatrix} \qquad (19)$$

The developed torque of a SynRM using i_{mq} and i_{md} can be expressed as:

$$T_e = \frac{3P}{4}(L_d - L_q)\,i_{mq}\,i_{md} \qquad (20)$$

Figure 15.
Basic characteristics of SynRM: (a) equivalent circuits considering iron loss and (b) phasors of voltages and currents neglecting core loss.

4.2.2.1 Motor losses

From **Figure 15b**, the copper loss P_{cu}, the core loss P_c, and the total loss P_t of a SynRM can be expressed as:

$$P_{cu} = \frac{3}{2} R_s \left(i_{qs}^2 + i_{ds}^2 \right), \ P_c = \frac{3}{2} R_c \left(i_{cq}^2 + i_{cd}^2 \right) \tag{21}$$

$$P_t = P_{cu} + P_c = \frac{3}{2} \left\{ \left[R_s + \frac{(\omega_e L_q)^2}{R_c} + \frac{(\omega_e L_q)^2 R_s}{R_c^2} \right] i_{mq}^2 + \left[R_s + \frac{(\omega_e L_d)^2}{R_c} + \frac{(\omega_e L_d)^2 R_s}{R_c^2} \right] i_{md}^2 \right.$$
$$\left. + \left[\frac{2R_s}{R_c} \omega_e (L_d - L_q) \right] i_{mq} i_{md} \right\} \tag{22}$$

By defining the variable $\varsigma = i_{mq}/i_{md}$, the commutation angle $\beta = \beta_o$ is derived to yield the minimum total loss P_t listed in Eq. (22):

$$\partial P_t / \partial \varsigma = 0, \ i_{mq} i_{md} = \text{constant} \tag{23}$$

Through derivation for Eq. (23) using Eq. (22), one can obtain:

$$\beta_o = \tan^{-1} \sqrt{\frac{\omega_e^2 L_d^2 (R_s + R_c) + R_s R_c^2}{\omega_e^2 L_q^2 (R_s + R_c) + R_s R_c^2}} \tag{24}$$

Comments: (i) from Eq. (24) one can find that by neglecting the core loss ($R_c = \infty$), the commutation angle will become $\beta = \beta_{o1} = 45°$; (ii) normally, $\beta > (\beta_{o1} = 45°)$ for pursuing the optimal efficiencies under varied operating conditions; (iii) as the commutation angle equation of Eq. (24) with nominal parameters of $(\overline{L}_d, \overline{L}_q, \overline{R}_c)$ is applied, the $(\beta = \beta_o) > 45°$ is resulted to yield better efficiency. If the accurate fitted parameters $(\hat{L}_d, \hat{L}_q, \hat{R}_c)$ are available to determine the value of $(\beta = \beta_o)$, a slightly increased efficiency may further be obtained.

4.3 Measurement of motor key parameters

4.3.1 Winding resistance and inductances

The estimations of these parameters are similar to those of PMSM described previously.

4.3.2 Estimation of iron core loss resistance R_c

a. As shown in **Figure 16**, the SynRM is driven under various speeds at no-load with the commutation shift angle of $\beta = 45°$. The input power P_{in} and motor line currents are measured. Then the copper loss P_{cu} can be calculated from Eq. (21), and the iron loss P_c can be obtained as $P_c = P_{in} - P_{cu}$.

b. The d-axis and q-axis voltages across R_c can be found from **Figure 15a** as:

$$V_{cd} = V_{ds} - I_{ds}R_s, \quad V_{cq} = V_{qs} - I_{qs}R_s \tag{25}$$

c. The equivalent resistance R_c can be obtained from Eq. (21) and **Figure 15a**:

$$P_c = \frac{3}{2}R_c\left(\left(\frac{V_{cd}}{R_c}\right)^2 + \left(\frac{V_{cq}}{R_c}\right)^2\right) \Rightarrow R_c = \frac{3}{2}\frac{\left(V_{cd}^2 + V_{cq}^2\right)}{P_c} \tag{26}$$

The estimated R_c are $\omega_r = 500$ rpm, $R_c = 34.71$ Ω; $\omega_r = 1000$ rpm, $R_c = 38.84$ Ω; $\omega_r = 1500$ rpm, $R_c = 54.34$ Ω; $\omega_r = 2000$ rpm, $R_c = 64.96$.

4.3.3 D-axis indexing

Taking an available three-phase SynRM (4-pole, 550 V, 2000 rpm, 3.7 kW, 17.67 Nm) as a test example, which is mechanically coupled with a three-phase PMSM (5 kW, 2000 rpm, 8-pole) as its dynamic load.

To verify the correctness of the detected rotor position, the AC voltage is injected into a-winding and b-winding terminals as indicated in **Figure 14b**. Owing to rotor saliency, a-phase current will be an amplitude modulated waveform. Let the PMSM be rotated at 100 rpm, the measured a-phase current i_{as}, Hall signal H_a, and rotor position θ_r due to the excited AC voltage 40 V/60 Hz which are plotted in
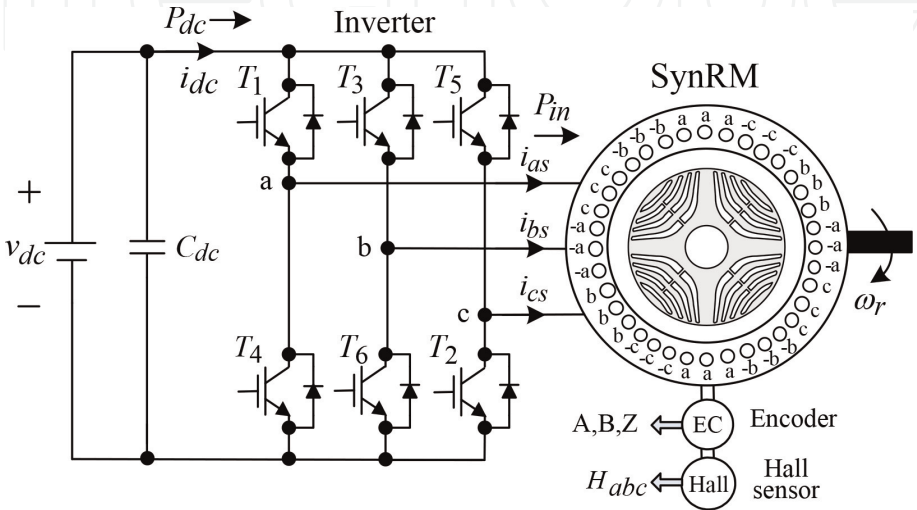
Figure 16.
Core loss resistance estimation mechanism.
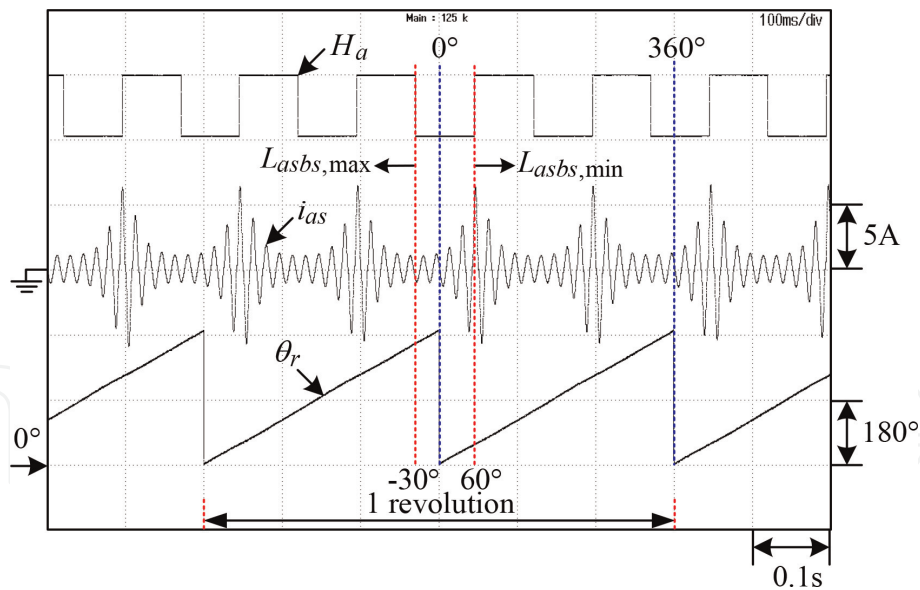
Figure 17.
Measured (H_a, i_{as}, θ_r) of an example of SynRM under excited AC voltage 40 V/60 Hz.
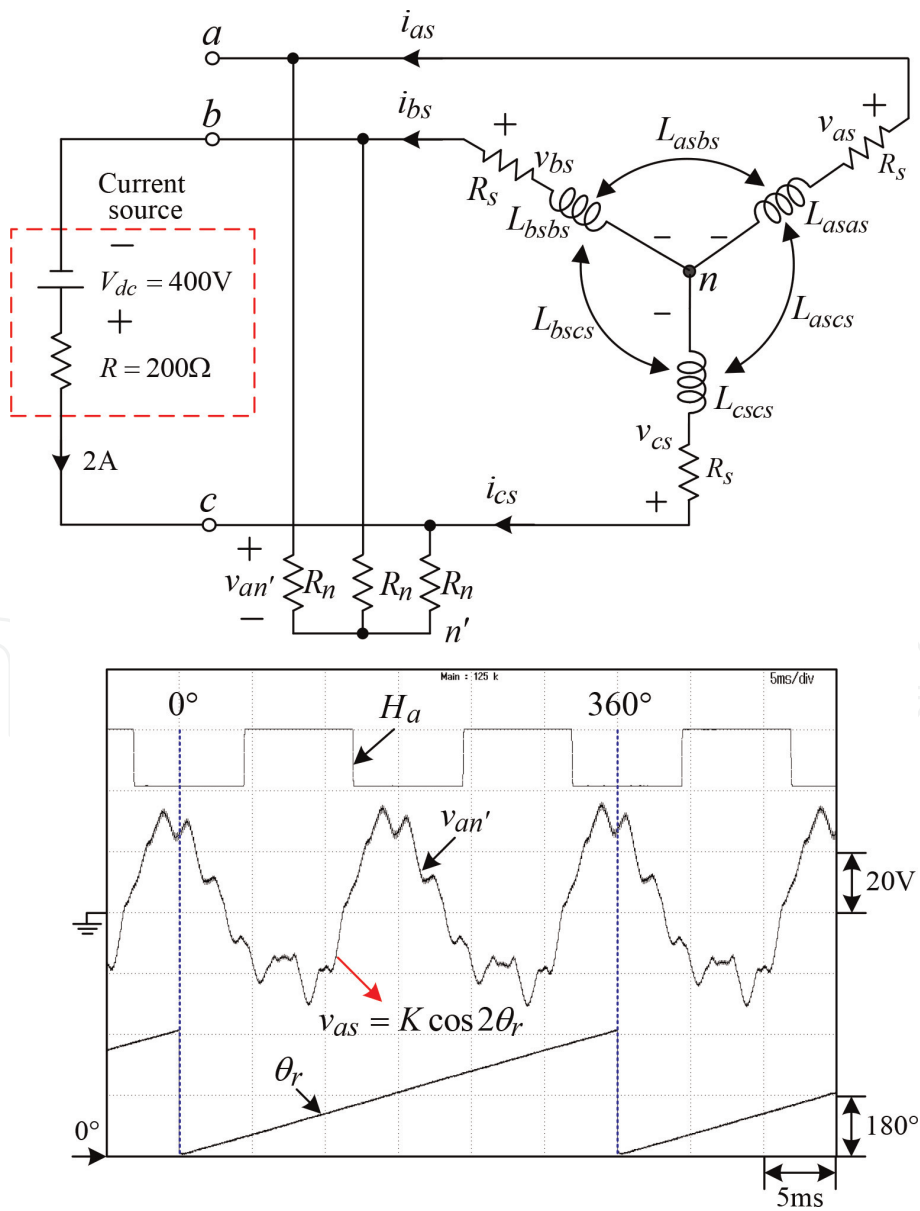
Figure 18.
Configuration of current-injected back-EMF measurement arrangement and the measured Hall signal, back-EMF, and rotor position.

Figure 17. It can be expected that the maximum and minimum current i_{as} occur at $L_{asbs,\,min}$ and $L_{asbs,\,max}$, respectively. From Eq. (10), the $L_{asbs,\,min}$ occurs at $\theta_r = \pi/3$, $L_{asbs,\,max}$ occurs at $\theta_r = -\pi/6$, and the $i_{as,\,max}$ and $i_{as,\,min}$ will also occur at $\theta_r = \pi/3$ and $\theta_r = -\pi/6$, respectively. Hence, from the measured waveforms in **Figure 17**, one can conclude that the detected rotor position is correct.

4.3.4 Back-EMF

From Eqs. (1), (3) and (15), one can find that SynRM possesses no back-EMF under no-load. As for the measurement mechanism proposed in **Figure 18**, a constant current is injected into the terminals c and b, and the a-phase terminal voltage $v_{as} \approx v'_{an}$ is detected and shown in **Figure 18**, which can be expressed using Eqs. (1) and (3) with $i_{bs} = -i_{cs} = I$ and $i_{as} = 0$ as:

$$v_{as} = \frac{d}{dt}\left(\sqrt{3}IL_B \sin 2\theta_r\right) = 2\sqrt{3}\omega_e IL_B \cos 2\omega_e t \underset{=}{\Delta} K \cos 2\theta_r, \quad \theta_r = \omega_e t \quad (27)$$

From the measured waveforms shown in **Figure 18**, one can be aware of some facts: (i) the adequacy of position sensing can be observed and (ii) the slotting effects can be comprehended from the ripples contaminated on $v_{an'}$.

4.4 Performance test of motor drive

Figure 19a and **b** shows the motor drive running characteristic test environment using eddy current brake and the suggested alternative test environment using load SPMSG as a dynamic load. Since the accurate eddy current brake and torque meter are not available, this alternative of loading test is worthy of adopting. However, the surface-mounted permanent-magnet synchronous generator (SPMSG) must be properly set, and it should be noted that the motor efficiency is both speed and load dependent.
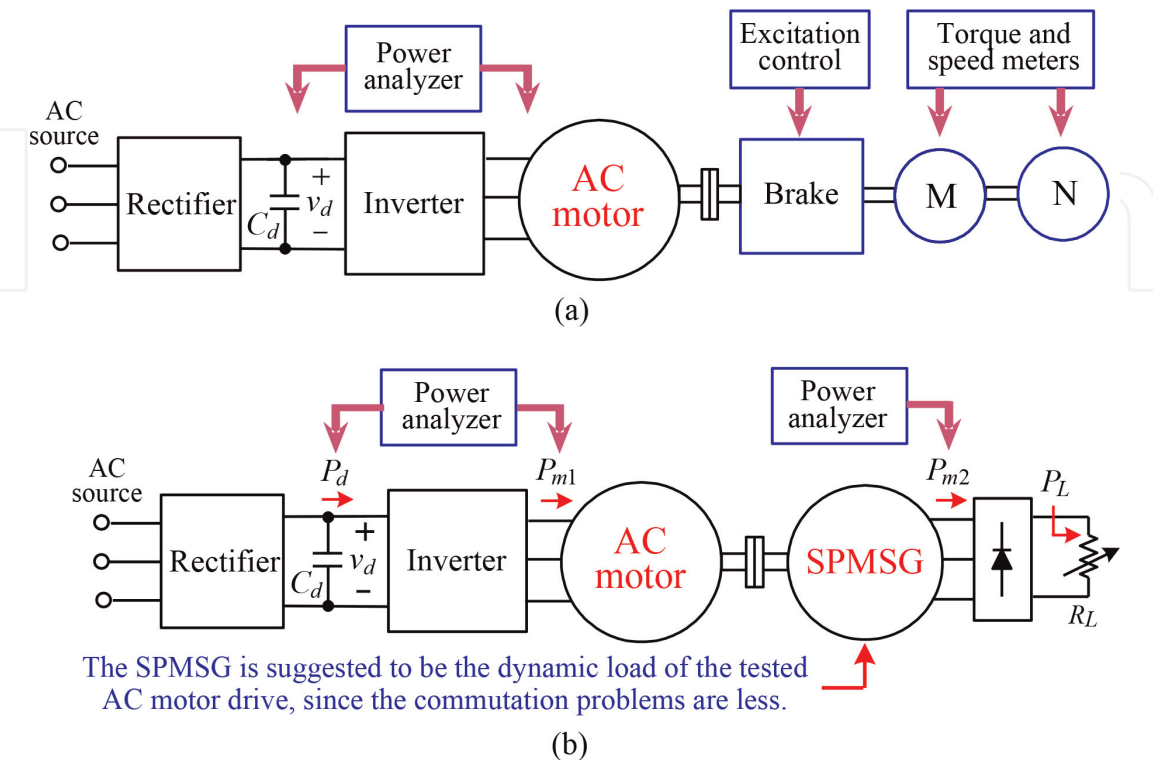
Figure 19.
Test facilities for AC motor drive: (a) running characteristic test using eddy current brake and (b) running characteristic test using load SPMSG as dynamic load.

5. A battery/supercapacitor-powered EV PMSM drive

5.1 System configuration

Figure 20a shows the developed battery/super-capacitor (SC)-powered electric vehicle (EV) IPMSM drive with proper interface power converters. The control scheme motor drive is shown in **Figure 20b**, whereas the control schemes of other power stages are neglected here.

5.1.1 IPMSM drive

5.1.1.1 System components

The used IPMSM is rated as three-phase 6-pole, 3000 rpm, 1 kW, 4.8 A, and 3.23 Nm. A surface-mounted PMSG is used as the dynamic load. The equipped dynamic brake leg is formed by (T_{B1}, R_B, D_{B1}) with the brake resistor $R_B = 25\ \Omega/200\ \text{W}$.

5.1.1.2 Operation control

a. Motoring mode: the positive torque current command i_{qs}^* yielded from the outer speed loop together with the properly set field excitation current command i_{ds}^* let the IPMSM to yield positive developed torque for driving control. The improved generated torque can be obtained by commutation advanced shift and voltage boosting. The d-axis current command is set to yield the maximum developed torque within rated speed:

$$i_{ds}^* = \frac{\lambda'_m}{2(L_q - L_d)} - \sqrt{\frac{(\lambda'_m)^2}{4(L_q - L_d)^2} + (i_{qs}^*)^2} \tag{28}$$

b. Regenerative braking: as the speed command is decreased, the negative speed tracking error ε_ω will let the torque current command i_{qs}^* become negative automatically. The recovered motor power will be sent back to charge the battery.

5.1.2 Battery interface converter

5.1.2.1 System components

The battery bank is formed by two serially connected cells (UC BATTERY PS 40138, 72 V 30 Ah) with nominal voltage $V_b = 156$ V. The DC-link voltage is arranged as $V_{dc,\,\text{min}} = 100$ V (buck mode), $V_{dc,\,\text{max}} = 400$ V (boost mode).

5.1.2.2 Operation control

5.1.2.2.1 Discharging mode

As shown in **Figure 20a**, through the H-bridge DC/DC converter, the battery ($v_b = 156$ V) establishes the adjustable and well-regulated DC-link voltage
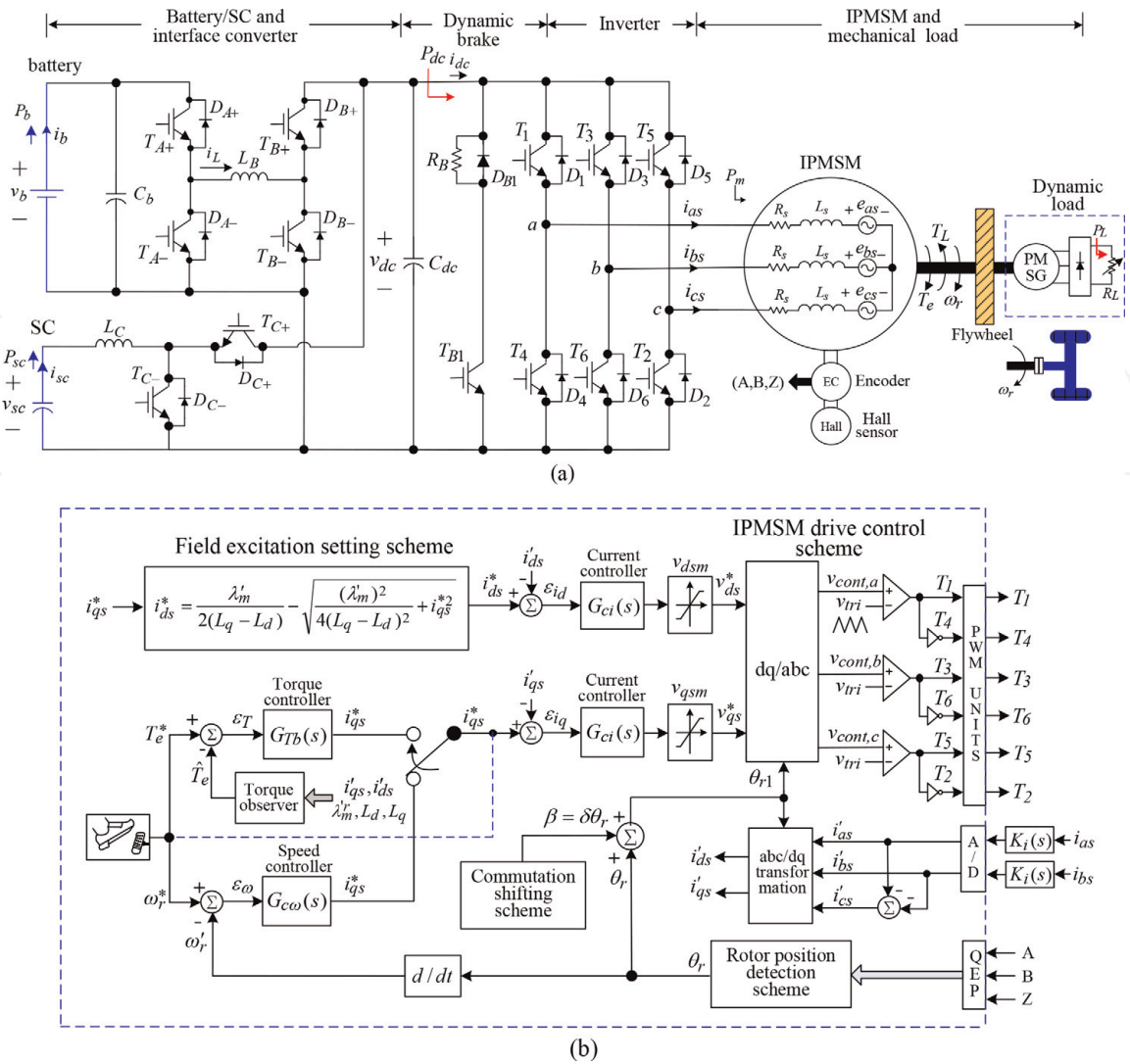
Figure 20.
The developed EV IPMSM drive: (a) schematic and (b) IPMSM drive control scheme.

($v_{dc} < v_b$ or $v_{dc} \geq v_b$). Here, the lowest and highest voltages are set as 100 V and 400 V, respectively. The buck converter is formed by ($T_{A+}, D_{A-}, L_B, D_{B+}$), while the boost converter is constructed using ($T_{A+}, T_{B+}, D_{B-}, L_B$).

5.1.2.2.2 Charging mode

In making battery charging during motor regenerative braking, the DC-link voltage is regulated at the set value, and the front-end converter is operated in reverse direction automatically. The components ($T_{B-}, D_{B+}, L_B, D_{A+}$) and ($T_{A-}, D_{A+}, L_B, T_{B+}$) form the buck and boost converters, respectively. The maximum battery charging current is equivalently set by $i_{Lm}^* = 12$ A of the current limiter.

5.1.3 SC interface converter

5.1.3.1 System components

The SC bank is rated as 6F/160 V, BMOD0006 E160 B02 (Maxwell Technologies), and maximum current = 170 V, maximum continuous current = 7 A, ESR (DC) = 240 $m\Omega$. The system voltage and power ratings are set as $V_{sc} = 100$ V, $V_{dc} = 400$ V, and $P_{dc} = 1$ kW.

5.1.3.2 Operation control

5.1.3.2.1 Motoring mode

In motoring mode, the DC-link voltage command v_{dc}^* of the SC is set slightly higher (405 V) than the nominal DC-link voltage V_{dc}(400 V). This will allow the switch T_{C-} be operated to discharge the SC stored energy for acceleration. Then the battery is discharged subsequently as the energy of SC is exhausted.

5.1.3.2.2 Regenerative braking mode

As the braking is commanded, the DC-link voltage will be larger than its command due to the recovered motor stored kinetic energy. Hence the negative value of voltage tracking error will let the current command of current loop in the SC energy storage system become negative. The switch T_{C+} will be operated to recycle the energy into the SC. Similarly, the maximum SC charging current is set by 20 A of the current limiter.

5.1.4 Adjustable DC-link voltage

For an inverter-fed motor drive, the lower DC-link voltage under lower speed and lighter load may yield smaller switching losses. Moreover, the EV is not often operated at relatively higher speed. As a result, the DC-link voltage can be properly set according to the motor running velocity to obtain higher efficiency over wide speed range. Most existing EV PCUs can only provide boosted motor drive DC-link voltage from battery. For the developed EV IPMSM drive, thanks to the flexibility possessed by the H-bridge DC/DC converter, the DC-link voltage can be lower than the battery voltage. The proposed DC-link voltage versus speed profile is depicted in **Figure 21**. The DC-link voltage profiles set for comparison are:

1. Fixed DC-link voltage: $v_{dc} = v_{dc1} = 400$ V, $0 \leq \omega_r \leq 4600$ rpm $(0 \leq \omega_r \leq \omega_m)$

2. Varied DC-link voltage:

    a. $v_{dc} = v_{dc2} = 100$ V, $0 \leq \omega_r \leq 1000$ rpm $(0 \leq \omega_r \leq \omega_1)$.

    b. 100 V $< (v_{dc} = v_{dc2}) \leq 400$ V, 1000 rpm $\leq \omega_r \leq 4600$ rpm $(\omega_1 < \omega_r \leq \omega_m)$
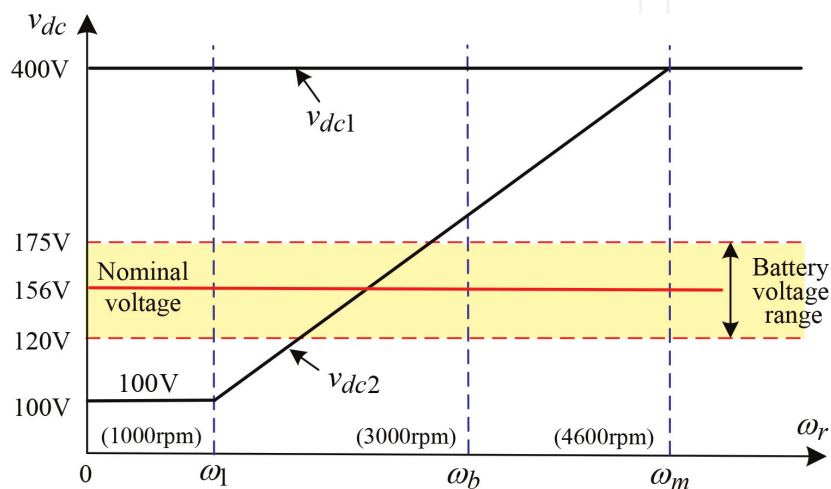
Figure 21.
The proposed DC-link voltage profile.

5.2 Some experimental results

5.2.1 Motor drive without SC

5.2.1.1 Steady-state characteristics

By setting i_{ds}^* according to Eq. (26), **Figure 22** shows the measured H_a and $(i_{as}^*, i_{as}, i_{ds}^*, i_{ds}')$ at $(v_b = 156$ V$, v_{dc} = 400$ V$, R_L = 44.7$ Ω$, \omega_r^* = 3000$ rpm$)$ of the developed EV IPMSM drive powered by battery H-bridge bidirectional DC/DC converter. The results show that the phase winding current commands i_{as}^* are properly shifted with respect to the sensed Hall signal H_a, and the i_{as}^* closely follows its command.

#### 5.2.1.2 Acceleration/deceleration/reversible and regeneration braking operation

Figure 23 shows the measured (ω_r^*, ω_r') and (i_{qs}^*, i_{qs}') at $(v_b = 156$V$, v_{dc} = 400$V$, R_L = 100.7$Ω$)$ of the EV IPMSM drive powered by H-bridge DC/DC front-end converter under forward and reversible operations, with the speed command being set as (3000 rpm) to (-3000 rpm) and the rate of 600 rpm/s. In order to let the IPMSM drive be reversibly operated, the torque current component is made opposite automatically, which can be seen from the results. The smooth speed forward and reversible operations can be seen from the results.

#### 5.2.1.3 Comparative evaluation for fixed and varied-voltage DC-links

The measured $(v_{dc}^*, v_{dc}', \omega_r^*, \omega_r', v_b, i_b, P_b, E_b)$ of the EV IPMSM drive powered by H-bridge DC/DC converter at $(R_L = 75$ Ω$)$ under the speed pattern defined by the ECE15. The speed pattern defined by ECE15 with fixed $v_{dc} = 400$ V and varied v_{dc} are compared in **Figure 24a** and **b**, where $P_b \equiv v_b \times i_b$ and $E_b \equiv \int P_b dt$. The developed EV IPMSM drives with fixed and varied v_{dc} all yield satisfactory driving characteristic.
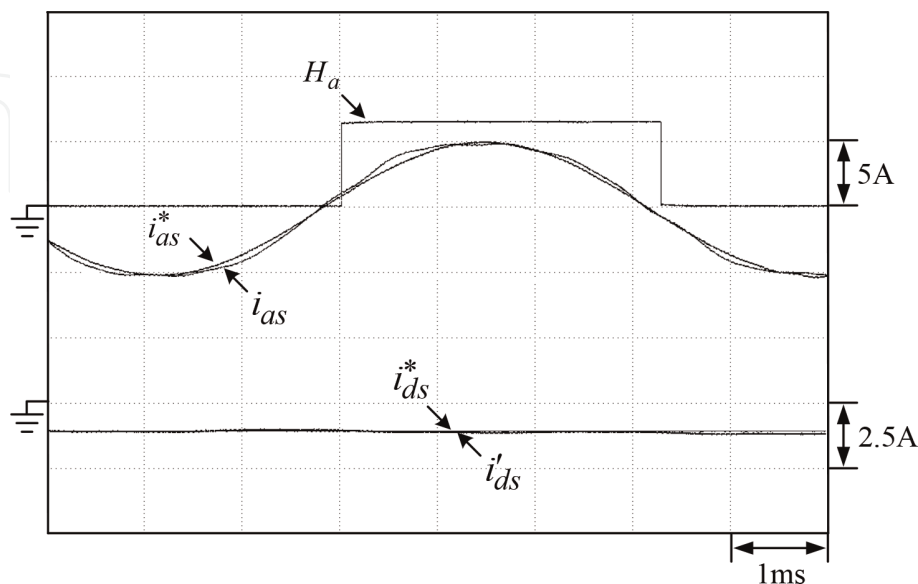
Figure 22.
Measured H_a and $(i_{as}^*, i_{as}, i_{ds}^*, i_{ds}')$ of the developed standard IPMSM drive powered by H-bridge DC/DC front-end converter at $(v_b = 156$ V$, \omega_r^* = 3000$ rpm$, R_L = 44.7$ Ω$)$ with $v_{dc} = 400$ V and $i_{ds}^* = -1$ A being set $(\hat{i}_{as} = 5.15A)$.
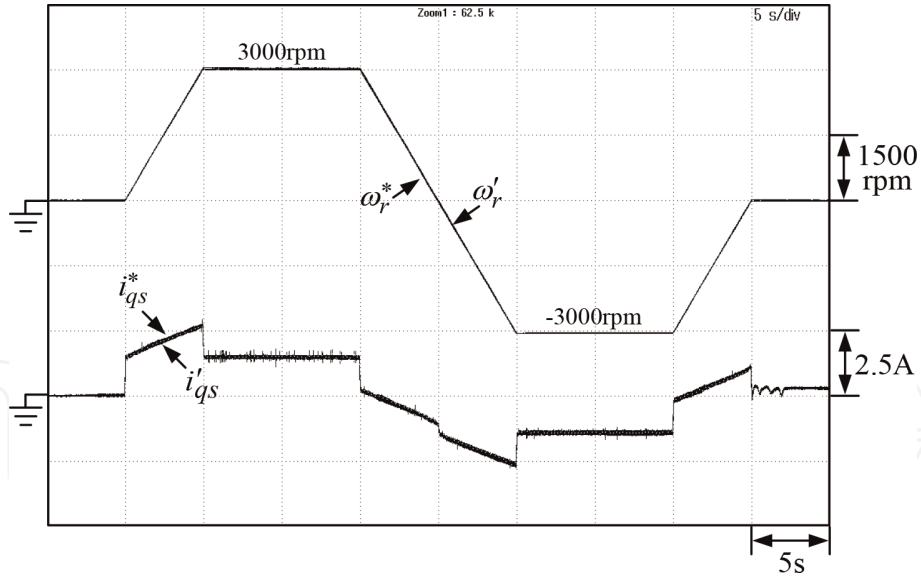
Figure 23.
Measured (ω_r^*, ω_r', i_{qs}^*, i_{qs}') of the developed IPMSM drive powered by H-bridge DC/DC front-end converter due to speed command change of ($\omega_r = 0$ rpm $\rightarrow$ 3000 rpm $\rightarrow$ 0 rpm $\rightarrow$ −3000 rpm $\rightarrow$ 0 rpm) under ($v_b = 156$ V, $v_{dc} = 400$ V, $R_L = 100.7$ Ω).
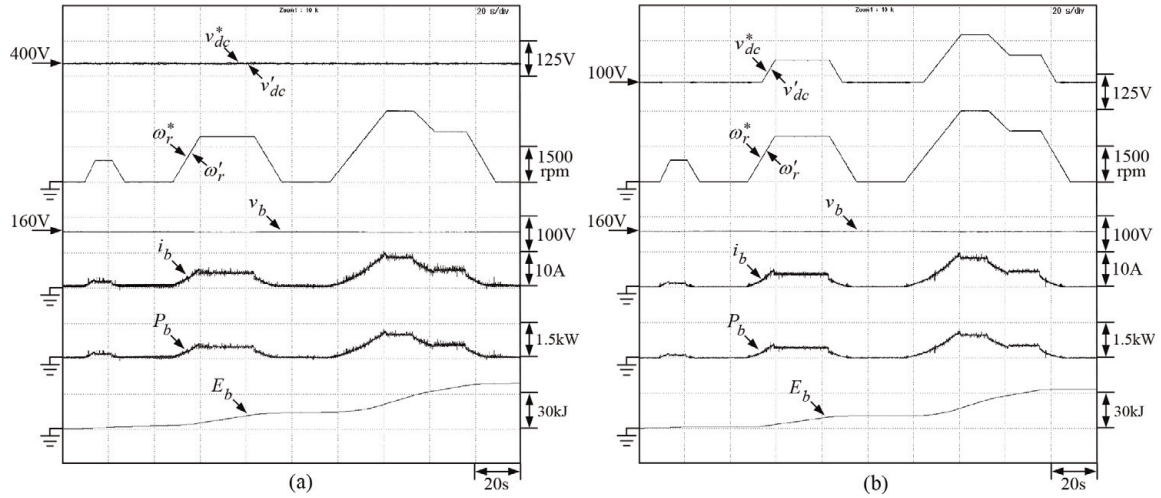
Figure 24.
Measured (v_{dc}^*, v_{dc}', ω_r^*, ω_r', v_b, i_b, P_b, E_b) of the developed EV IPMSM drive powered by H-bridge DC/DC front-end converter at ($R_L = 75$ Ω) due to the speed pattern defined by the ECE15: (a) v_{dc} is fixed at 400 V and (b) v_{dc} is varied with speed.

The measured E_b by the fixed v_{dc} and the varied v_{dc} corresponding to **Figure 24** are further compared in **Figure 25**. From the comparison one can find that the adjustable DC-link voltage can reduce battery energy consumption.

5.2.2 Motor drive incorporated with SC

Under the preset speed changing pattern as shown in **Figure 26**, the measured results of the established EV IPMSM drive powered by H-bridge DC/DC front-end converter with acceleration and deceleration rates of 750 rpm/s at ($v_b = 156$ V, $v_{dc}^* = 400$ V, $v_{sc}^* = 405$ V, $R_L = 75$ Ω) are provided as: **Figure 26a**: (ω_r^*, ω_r', i_b, v_b, v_{dc}) without SC; Figure **26b**: (ω_r^*, ω_r', i_b, i_{sc}, v_{sc}, v_b, v_{dc}) with SC. Without SC, the battery possesses larger charging and discharging currents as shown in Figure **26a**.

The application of SC can reduce the battery currents in driving and regenerative braking operations under the same scenario. In the results presented in **Figure 26b** with SC using active discharging approach (noted that $v_{sc}^* > v_{dc}^*$), the battery current remains zero at the beginning under driving mode, the SC
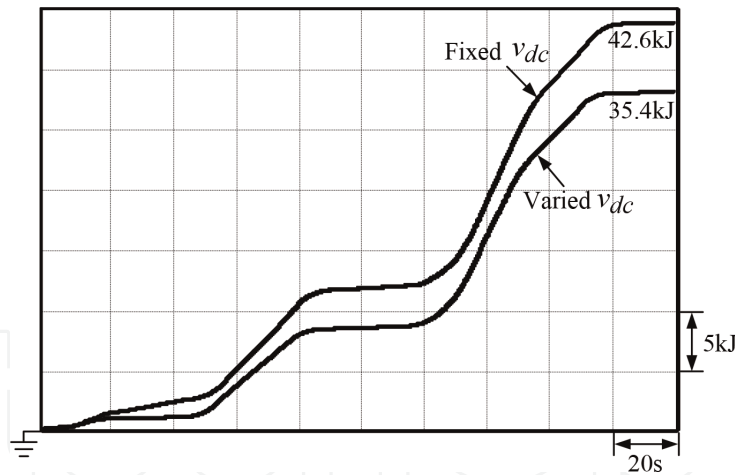
Figure 25.
Measured E_b of the developed standard IPMSM drive powered by H-bridge converter with fixed $v_{dc} = 400$ V and varied v_{dc} due to speed pattern defined by the ECE15 at ($R_L = 75$ Ω).
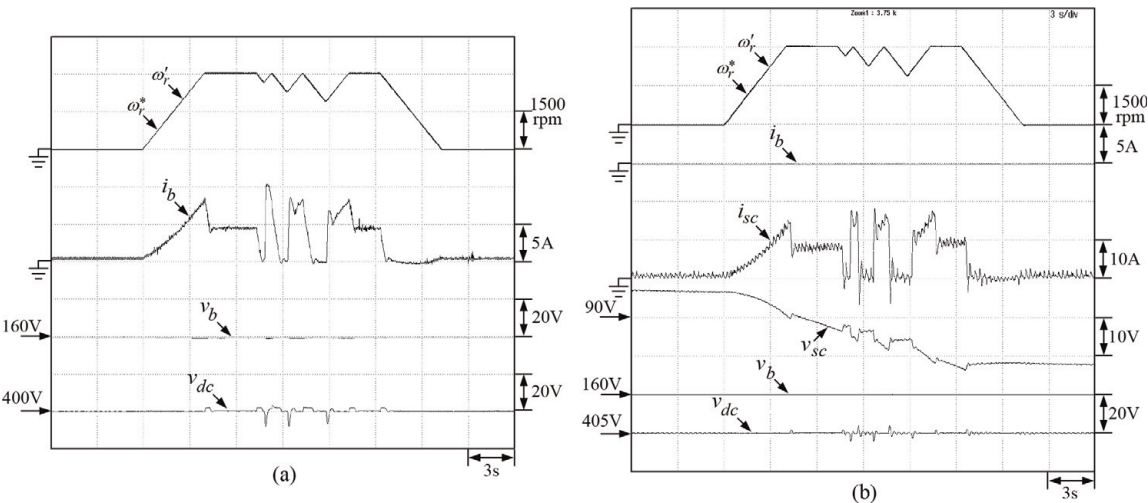
Figure 26.
Measured results of the established standard EV IPMSM drive powered by H-bridge DC/DC front-end converter due to preset speed pattern with acceleration and deceleration rates of 750 rpm/s at $(v_b = 156$ V, $v_{dc}^* = 400$ V, $v_{sc}^* = 405$ V, $R_L = 75$ Ω): (a) $((\omega_r^*, \omega_r'), i_b, v_b, v_{dc})$ without SC and (b) $((\omega_r^*, \omega_r'), i_b, i_{sc}, v_{sc}, v_b, v_{dc})$ with SC under discharging operation.

discharges via its bidirectional converter first, and the battery pack does not supply power to DC link until the SC is unable to maintain the driving torque. Hence, not only the energy of regenerative braking can be recycled, but also the battery can avoid its intermittent charging/discharging operations. Obviously, by adding the supercapacitor storage system, the battery provides the fewer power during acceleration condition, and its current would never become negative. Besides, the battery voltage is also less fluctuated.

6. A bidirectional SMR-fed synchronous reluctance motor drive

6.1 System configuration

Figure 27a shows the developed SMR-fed SynRM drive. And the control scheme of the motor drive is depicted in **Figure 27b**. The three-phase full-bridge SMR is employed to power the motor drive from the mains with good line drawn power quality. The boosted and well-regulated DC-link voltage enhances motor driving performance over wide speed range. Moreover, the recovered energy during regenerative braking can be successfully sent back to utility grid.
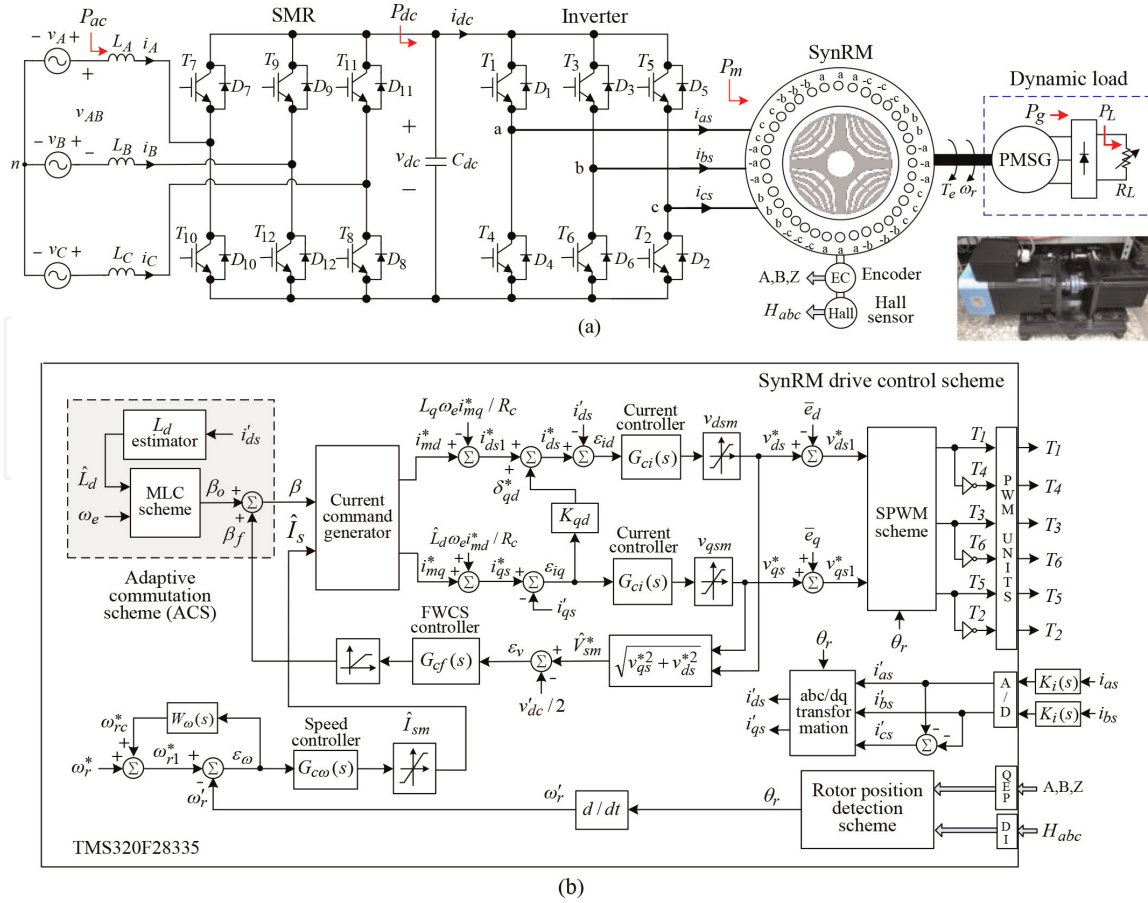
Figure 27.
The SMR-fed SynRM drive: (a) schematic and (b) motor drive control scheme.

In treating the driving control for a SynRM drive, some distinct features are worth noting: (i) since only reluctance torque is exited, the proper commutation angle setting is the most critical issue affecting its developed torque characteristics; (ii) the iron loss of SynRM is significant and varied with operating conditions; and (iii) the d-axis inductance is significantly changed with the armature current level due to magnetic saturation; hence, the iron loss and copper loss should be simultaneously considered to yield the improved overall efficiency. In the SynRM drive control scheme shown in **Figure 27b**, the proposed improved approaches include (i) the commutation angle is set by an adaptive commutation scheme (ACS) using online estimated d-axis inductance to minimize motor total loss. Under higher speed, an extra commutation angle is yielded by the field-weakening commutation scheme (FWCS) to limit the voltage. And (ii) in the proposed ramp-comparison current-controlled PWM (RC-CCPWM) scheme, the basic feedback control is augmented with a back-EMF elimination feedforward controller and a transient cross-coupling field controller to enhance the current control performance.

6.1.1 SynRM drive

6.1.1.1 System components

a. The employed SynRM is rated as SynRM: 4-pole, 550 V, 2000 rpm, 3.7 kW. The inverter is formed using three Mitsubishi IGBT modules CM100DY-12H ($V_{CE} = 600$ V, $I_C = 100$ A, $I_{CM} = 200$ A). The SPWM switching is employed. A PMSG with load resistanceR_L is served as the dynamic load of the studied SynRM.

b. Estimated motor parameters: $R_s = 0.47$ Ω, $R_c = 61.37$ Ω, $L_q = 28.92$ mH (at 66.6 Hz). The d-axis inductance L_d is much affected by the magnetic saturation compared to the q-axis inductance L_q. The fitted $\hat{L}_d(i_{md})$ (in H) is expressed as:

$$\hat{L}_d(i_{md}) = \begin{cases} 0.0559 \ (\text{H}), & i_{md} \leq 3\text{A} \\ \alpha_1 \ln \ (i_{md}) + \alpha_2 \ (\text{H}), & i_{md} > 3\text{A} \end{cases} \tag{29}$$

where $\alpha_1 = -0.00864$ and $\alpha_2 = -0.06458$.

6.1.1.2 Commutation scheme

a. The proposed adaptive commutation scheme (ACS): the fitted $\hat{L}_d(i_{md})$ and the estimated motor parameters are applied to Eq. (24) to determine the commutation angle $(\beta = \beta_o)$.

b. Field-weakening commutation scheme (FWCS)

Under higher speeds, the field weakening via commutation advanced shift must be applied to satisfy the electrical capabilities of a SynRM drive expressed as:

$$\hat{I}_s = \sqrt{i_{qs}^2 + i_{ds}^2} \leq \hat{I}_{sm} \tag{30}$$

$$\hat{V}_s = \sqrt{v_{qs}^2 + v_{ds}^2} \leq \hat{V}_{sm} = v_{dc}/2 \tag{31}$$

where $\hat{I}_s$ $(\hat{V}_s)$ = phase current (voltage) magnitude and the maximum voltage $\hat{V}_{sm} = v_{dc}/2$ is set for a SPWM inverter.

For regulating the voltage limit automatically, the commutation shift angle β_f is yielded by the proposed FWCS scheme shown in **Figure 27b** as:

$$\beta_f = \begin{cases} 0, & \sqrt{v_{qs}^{*2} + v_{ds}^{*2}} < \left(\dfrac{v'_{dc}}{2}\right) \\ G_{cf}(s)\left(\sqrt{v_{qs}^{*2} + v_{ds}^{*2}} - \left(\dfrac{v'_{dc}}{2}\right)\right), & \sqrt{v_{qs}^{*2} + v_{ds}^{*2}} \geq \left(\dfrac{v'_{dc}}{2}\right) \end{cases} \tag{32}$$

6.1.2 Three-phase full-bridge SMR

To simultaneously preserve bidirectional power flow and power factor corrected capabilities, the three-phase full-bridge SMR is established and employed as the AC front end of the SynRM drive. The three-phase AC input line voltage is 220 V/ 60 Hz. And the DC-link voltage is set as $V_{dc} = 550$ V. Three IGBT modules CM100DY-12H are used to form the power circuit.

6.2 Some experimental results

6.2.1 Performance of SMR front end

Figure 28a and **b** shows the steady-state characteristics of the three-phase full-bridge SMR-fed SynRM drive at $(V_{dc} = 550$ V, $\omega_r = 2000$ rpm, $\beta = \beta_{o1} = 45°$, $R_L = 13.7Ω)$. The results indicate that the SMR possesses good operating
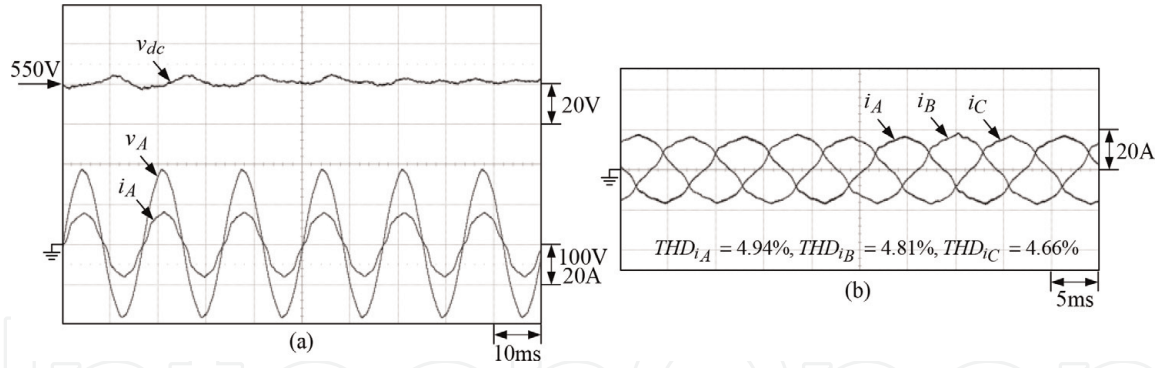
Figure 28.
Measured steady-state results of the developed SMR-fed SynRM drive under (V_{dc} = 550 V, ω'_r = 2000 rpm, β = 45°, R_L = 13.7 Ω): (a) (v_{dc}, v_A, i_A) and (b) (i_A, i_B, i_C).

characteristics in powering the followed SynRM drive, good line drawn power quality, and well-regulated DC-link voltage which are seen.

### 6.2.2 Effectiveness of the proposed ACS scheme

Under (V_{dc} = 550 V, R_L = 13.7 Ω), let the commutation angles be $\beta = \beta_{o1} = 45°$ and $\beta = \beta_o$ yielded from Eq. (24); the measured (ω'_r, $\hat{I}_s$, P_{dc}) of the SynRM drive at two speeds are compared in **Figure 29a** and **b**. One can find that the proposed commutation angle setting can lead to less power consumption and the reduction of current magnitude.

### 6.2.3 Effectiveness of the proposed FWCS in high-speed driving performance

Since the rated speed of the used SynRM is 2000 rpm, the proper field weakening is necessary under the speeds larger than 2000 rpm. Let the commutation angle be $\beta = \beta_{o1} + \beta_f$ with β_{o1} = 45° being set and β_f being yielded by the developed FWCS. **Figure 30** plots the measured (ω^*_r, ω'_r) and the yielded commutation angle β_f during starting process at (V_{dc} = 550 V, R_L = 303.9 Ω) from 0 to 4000 rpm with an acceleration rate of (250 rpm/s). One can find from the results that speed tracking error under high speeds can be eliminated by applying the FWCS via increasing the commutation angle component β_f.

6.2.4 Reversible operation

The measured (ω^*_r, ω'_r) and $\hat{I}_s$ of the SMR-fed SynRM drive at (V_{dc} = 550 V, R_L = 13.7 Ω) with the commutation angle $\beta = \beta_o$ due to the ramp
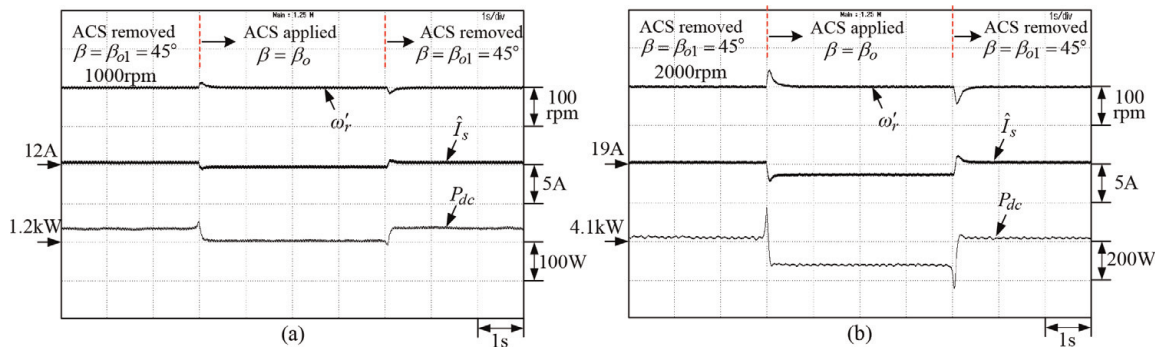
Figure 29.
Measured (ω'_r, $\hat{I}_s$, P_{dc}) of the established SMR-fed SynRM drive with $\beta = \beta_{o1}$ = 45° and $\beta = \beta_o$ by the proposed ACS under (V_{dc} = 550 V, R_L = 13.7 Ω): (a) ω'_r = 1000 rpm and (b) ω'_r = 2000 rpm.
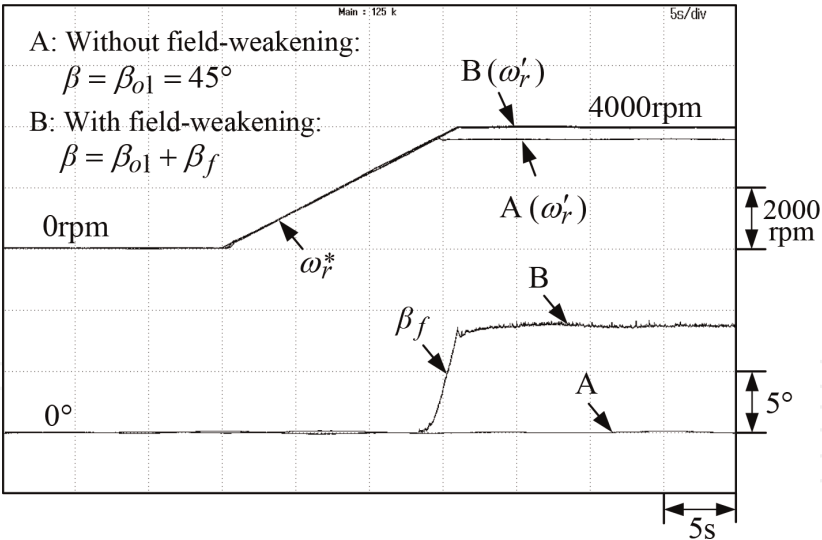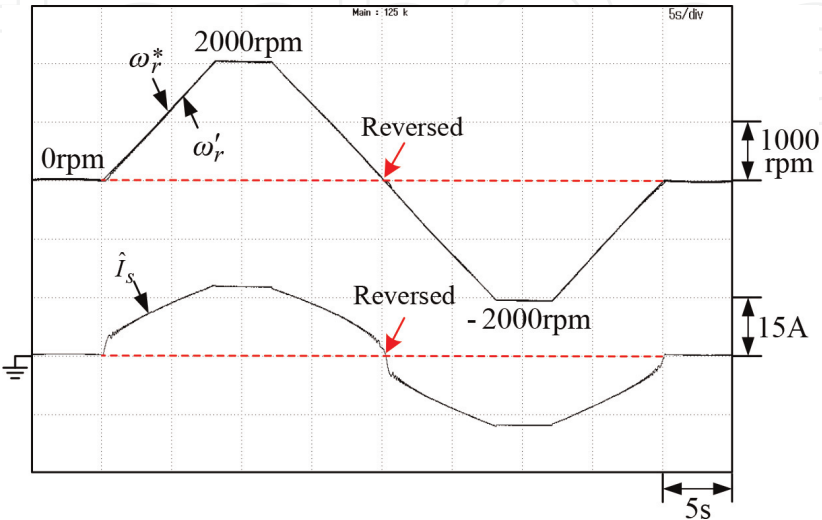
Figure 30.
Measured (ω_r^*, ω'_r) and the commutation angle β_f yielded by the FWCS during starting process from 0 to 4000 rpm at ($V_{dc} = 550$ V,$R_L = 303.9$ Ω).

speed command change $\omega_r^* = 0 \rightarrow 2000$ rpm $\rightarrow 0 \rightarrow -2000$ rpm $\rightarrow 0$ with the rising and falling rates of 250 rpm/s being plotted in **Figure 31**. The results indicate the smooth speed tracking and reversible operation of the developed SynRM drive.

6.2.5 Regenerative braking

The SynRM drive is first stably operated at ($\omega'_r = 2000$ rpm, $V_{dc} = 550$ V, $R_L = \infty$). Now the speed command is set from $\omega_r^* = 2000$ rpm to 0 rpm linearly in 1 s. The measured DC-link voltage $v_{dc}(\omega_r^*, \omega'_r)$, $\hat{I}_s$ and phase-a winding current are of the established SMR-fed SynRM drive which are plotted in **Figure 32a**. One can be aware of the results that the current command $\hat{I}_s$ becomes negative under regenerative braking operation. Successful SynRG operation during regenerative braking is confirmed. And **Figure 32b** shows the DC-link voltage v_{dc}, phase-A voltage v_A, and current i_A of the mains. From **Figure 32b**, the regenerative braking of SynRM drive with energy recovered back to the mains can be observed.

Figure 31.
Measured (ω_r^*, ω'_r) and $\hat{I}_s$ of the SynRM drive at ($V_{dc} = 550$ V,$R_L = 13.7$ Ω) with $\beta = \beta_o$ due to ramp speed command change $\omega_r^* = 0 \rightarrow 2000$ rpm $\rightarrow 0 \rightarrow -2000$ rpm $\rightarrow 0$ with both the rising rate and falling rate being 250 rpm/s.
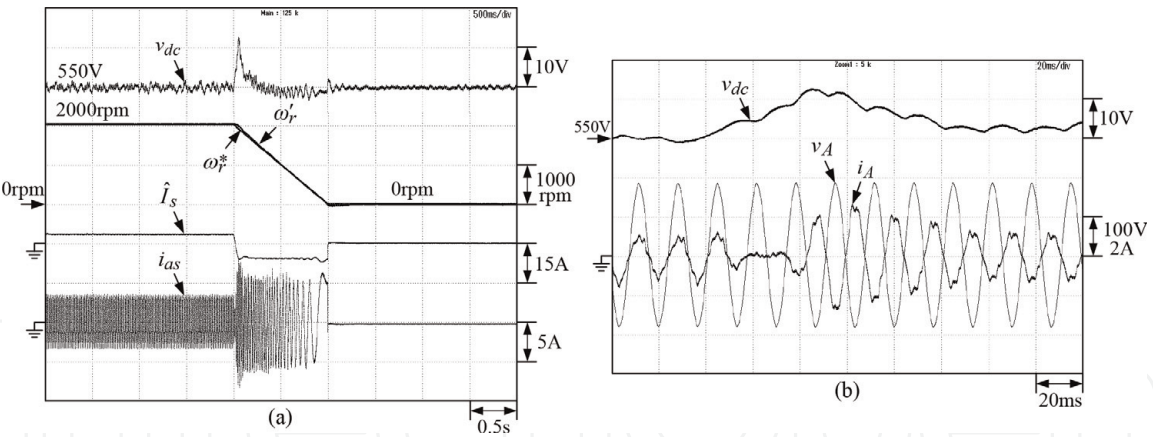
Figure 32.
Measured results of the established SMR-fed SynRM drive during braking by letting the speed command be changed from $\omega_r^* = 2000$ rpm to 0 rpm linearly in 1 s: (a) DC-link voltage v_{dc}, (ω_r^*, ω_r'), current command $\hat{I}_s$, and a-phase winding current, i_{as} and (b) DC-link voltage v_{dc}, A-phase voltage, and current (v_A, i_A) from the mains.

6.2.6 Efficiency evaluation

In order to verify the efficiency enhancement of the established SMR-fed SynRM drive using the proposed ACS, the measured steady-state characteristics at $(V_{dc} = 550$ V, $R_L = 13.7$ Ω, $\omega_r' = 2000$ rpm) with the commutation angles $\beta = \beta_{o1} = 45°$ and $\beta = \beta_o$ yielded by the proposed ACS are listed in **Table 1**. The efficiencies are defined as:

$\eta_{SMR} \equiv P_{dc}/P_{ac} =$ SMR efficiency, $\eta_m \equiv$ SynRM efficiency,
$\eta_g \equiv$ load PMSG efficiency, $\eta_1 \equiv P_L/P_{dc} = (P_m/P_{dc})(P_g/P_m)(P_L/P_g)$, and
$\eta \equiv \eta_{SMR}\eta_1 = P_L/P_{ac} =$ total efficiency.

The improvement in energy conversion efficiency via the proposed ACS is obvious from the results. The high efficiency possessed by the developed SynRM drive can also be aware.

Speed	$\beta = \beta_{o1} = 45°$			$\beta = \beta_o$ by ACS		
2000 rpm	P_L = 3253.8 W			P_L = 3251.7 W		
	P_{dc} = 4064.3 W			P_{dc} = 3980.1 W		
	P_{ac} = 4380.0 W			P_{ac} = 4285.0 W		
	PF = 0.998		THD_{i_A} = 5.05%	PF = 0.997		THD_{i_A} = 4.98%
	η_{SMR} = 92.8%	η_1 = 80.1%	η = 74.3%	η_{SMR} = 92.9%	η_1 = 81.7%	η = 75.9%

Table 1.
Measured steady-state characteristics of the established SMR-fed SynRM drive at $(V_{dc} = 550$ V, $R_L = 13.7$ Ω, $\omega_r' = 2000$ rpm).

7. Conclusions

As generally recognized, PMSM and SynRM are the two new motors having the potential to achieve the IE4-class and even the IE5-class efficiency. During the past years, the popularly used induction motors have been gradually replaced by these two motors in various applications, such as home appliances, EVs, wind generators, etc. For facilitating the development of high-performance PMSM and SynRM drives, this article has presented some basics and key affairs. Moreover, an example

of EV PMSM drive and an example of SMR-fed SynRM drive have also been introduced for demonstration. Generally speaking, the most critical issues lie in (i) selecting suited type of motor for specific applications, (ii) proper commutation instant setting and shifting, (iii) applying DC-link voltage boosting approach to enhance high-speed driving characteristics, and (iv) properly conducting the regenerative braking operation control.

Author details

Chang-Ming Liaw*, Jia-Hsiang Zhuang, Shih-Wei Su, Kai-Wei Hu
and G. Vijay Kumar
Department of Electrical Engineering, National Tsing Hua University, Hsinchu,
Taiwan, ROC

*Address all correspondence to: cmliaw@ee.nthu.edu.tw

IntechOpen

References

[1] Krause PC, Wasynczuk O, Sudhoff SD. Analysis of Electric Machinery and Drive System. 2nd ed. New York: Wiley-IEEE; 2002

[2] Murakami H, Honda Y, Kiriyama H, Morimoto S, Takeda Y. The performance comparison of SPMSM, IPMSM and SynRM in use as air-conditioning compressor. In: Proceedings of IEEE IAS; 1999. pp. 840-845

[3] Murakami H, Honda Y, Morimoto S, Takeda Y. Permanent magnet assisted synchronous reluctance motor. IEEJ Transactions on Industry Applications. 2002;**122**(3):266-272

[4] Zeraoulia M, Benbouzid MEH, Diallo D. Electric motor drive selection issues for HEV propulsion systems: A comparative study. IEEE Transactions on Vehicular Technology. 2006;**55**(6): 1756-1764

[5] Morimoto S. Trend of permanent magnet synchronous machines. IEEJ Transactions on Electrical and Electronic Engineering. 2007;**2**(2): 101-108

[6] Pellegrino G, Vagati A, Boazzo B, Guglielmi P. Comparison of induction and PM synchronous motor drives for EV application including design examples. IEEE Transactions on Industry Applications. 2012;**48**(6): 2322-2332

[7] Bostanci E, Moallem M, Parsapour A, Fahimi B. Opportunities and challenges of switched reluctance motor drives for electric propulsion: A comparative study. IEEE Transactions on Transportation Electrification. 2017; **3**(1):58-75

[8] Weisgerber S, Proca A Keyhani A. Estimation of permanent magnet motor parameters. Proceedings of IEEE IAS. 1997;**1**(1):29-34

[9] Kondo M. Parameter measurements for permanent magnet synchronous machines. IEEJ Transactions on Electrical and Electronic Engineering. 2007;**2**(2):109-117

[10] Kazmierkowski MP, Malesani L. Current control techniques for three phase voltage-source PWM converters: A survey. IEEE Transactions on Industrial Electronics. 1998;**45**(5): 691-703

[11] Chou MC, Liaw CM, Chien SB, Shien FH, Tsai JR, Chang HC. Robust current and torque controls for PMSM driven satellite reaction wheel. IEEE Transactions on Aerospace and Electronic Systems. 2011;**47**(1):58-74

[12] Siami M, Khaburi DA, Abbaszadeh A, Rodriguez J. Robustness improvement of predictive current control using prediction error correction for permanent-magnet synchronous machines. IEEE Transactions on Industrial Electronics. 2016;**63**(6): 3458-3466

[13] Sawma J, Khatounian F, Monmasson E, Idkhajine L, Ghosn R. Analysis of the impact of online identification on model predictive current control applied to permanent magnet synchronous motors. IET Electric Power Applications. 2017; **11**(5):864-873

[14] Preindl M, Bolognani S. Model predictive direct speed control with finite control set of PMSM drive systems. IEEE Transactions on Power Electronics. 2013;**28**(2):1007-1015

[15] Jung JW, Leu VQ, Do TD, Kim EK, Choi HH. Adaptive PID speed controller design for permanent magnet synchronous motor drives. IEEE Transactions on Power Electronics. 2015;**30**(2):900-908

[16] Sant AV, Rajagopal KR. PM synchronous motor speed control using

hybrid fuzzy-PI with novel switching functions. IEEE Transactions on Magnetics. 2009;**45**(10):4672-4675

[17] Lukichev DV, Demidova GL. Speed control in PMSM drive with non-stiff load and unknown parameters using PI—And fuzzy adaptive PID controllers. In: 2017 International Conference on Industrial Engineering, Applications and Manufacturing (ICIEAM); 2017. pp. 1-5

[18] Justo JJ, Mwasilu F, Kim EK, Kim J, Choi HH, Jung JW. Fuzzy model predictive direct torque control of IPMSMs for electric vehicle applications. IEEE/ASME Transactions on Mechatronics. 2017;**2**(4):1542-1553

[19] Mohamed YA-RI, Lee TK. Adaptive self-tuning MTPA vector controller for IPMSM drive system. IEEE Transactions on Energy Conversion. 2006;**21**(3):636-644

[20] Niazi P, Toliyat HA, Goodarzi A. Robust maximum torque per ampere (MTPA) control of PM-assisted SynRM for traction applications. IEEE Transactions on Vehicular Technology. 2007;**56**(4):1538-1545

[21] Chen HC Liaw CM. Sensorless control via intelligent commutation tuning for brushless DC motor. Proceedings of IEE Electric Power Applications. 1999;**146**(6):678-684

[22] Chen HC, Liaw CM. Current-mode control for sensorless BDCM drive with intelligent commutation tuning. IEEE Transactions on Power Electronics. 2002;**17**(5):747-756

[23] Liaw CC, Liaw CM, Chang HC, Huang MS. Robust current control and commutation tuning for an IPMSM drive. Proceedings of IEEE APEC. 2003;**2**(2):1045-1051

[24] Sato E. Permanent magnet synchronous motor drives for hybrid electric vehicles. Transactions on Electrical and Electronic Engineering. 2007;**2**(2):162-168

[25] Bolognani S, Calligaro S, Petrella R. Adaptive flux-weakening controller for interior permanent magnet synchronous motor drives. IEEE Journal of Emerging and Selected Topics in Power Electronics. 2014;**2**(2):236-248

[26] Burress T. Benchmarking EV and HEV technologies. Technical Report ORNL; 2015

[27] Chou MC, Liaw CM. PMSM-driven satellite reaction wheel system with adjustable DC-link voltage. IEEE Transactions on Aerospace and Electronic Systems. 2014;**50**(2):1359-1373

[28] Liaw CM, Hu KW, Lin YS, Yeh TH. An electric vehicle IPMSM drive with interleaved front-end DC/DC converter. IEEE Transactions on Vehicular Technology. 2016;**65**(6):4493-4504

[29] Garcia O, Cobos JA, Prieto R, Alou P, Uceda J. Single phase power factor correction: A survey. IEEE Transactions on Power Electronics. 2003;**18**(3):749-755

[30] Singh B, Singh NB, Chandra A, Haddad KA, Pandey A, Kothari PD. A review of three-phase improved power quality AC/DC converters. IEEE Transactions on Industrial Electronics. 2004;**51**(3):641-660

[31] Friedli T, Kolar JW. The essence of three-phase PFC rectifier systems part I. IEEE Transactions on Power Electronics. 2013;**28**(1):176-198

[32] Yilmaz M, Krein PT. Review of battery charger topologies, charging power levels, and infrastructure for plug-in electric and hybrid vehicles. IEEE Transactions on Power Electronics. 2013;**28**(5):2151-2169

[33] Matsui N. Sensorless PM brushless DC motor drives. IEEE Transactions on Industrial Electronics. 1996;**43**(2): 300-308

[34] Johnson JP, Ehsani M, Guzelgunler Y. Review of sensorless methods for brushless DC. Proceedings of IEEE IAS. 1999;**1**:143-150

[35] Sul SK, Kwon YC, Lee Y. Sensorless control of IPMSM for last 10 years and next 5 years. CES Transactions on Electrical Machines and Systems. 2017; **1**(2):91-99

[36] Hamida MA, Leon JD, Glumineau A, Boisliveau R. An adaptive interconnected observer for sensorless control of PM synchronous motors with online parameter identification. IEEE Transactions on Industrial Electronics. 2013;**60**(2):739-748

[37] Rafaq MS, Mwasilu F, Kim J, Choi HH, Jung JW. Online parameter identification for model-based sensorless control of interior permanent magnet synchronous machine. IEEE Transactions on Power Electronics. 2017;**32**(6):4631-4643

[38] Jang JH, Ha JI, Ohto M, Ide K, Sul SK. Analysis of permanent-magnet machine for sensorless control based on high-frequency signal injection. IEEE Transactions on Industry Applications. 2004;**40**(6):1595-1604

[39] Guerrero JM, Leetmaa M, Briz F, Zamarron A, Lorenz RD. Inverter nonlinearity effects in high-frequency signal-injection-based sensorless control methods. IEEE Transactions on Industry Applications. 2005;**41**(2):618-626

[40] Raca D, Garcia P, Reigosa DD, Briz F, Lorenz RD. Carrier-signal selection for sensorless control of PM synchronous machines at zero and very low speeds. IEEE Transactions on Industry Applications. 2010;**46**(1): 167-178

[41] Andreescu GD Schlezinger C. Enhancement sensorless control system for PMSM drives using square-wave signal injection. In: Proceedings of IEEE SPEEDAM. 2010. pp. 1508-1511

[42] Kim D, Kwon YC, Sul SK, Kim JH, Yu RS. Suppression of injection voltage disturbance for high-frequency square-wave injection sensorless drive with regulation of induced high-frequency current ripple. IEEE Transactions on Industry Applications. 2016;**53**(1): 302-312

[43] Po-ngam S, Sangwongwanich S. Stability and dynamic performance improvement of adaptive full-order observers for sensorless PMSM drive. IEEE Transactions on Power Electronics. 2012;**27**(2):588-600

[44] Park Y, Sul SK. Sensorless control method for PMSM based on frequency-adaptive disturbance observer. IEEE Journal of Emerging and Selected Topics in Power Electronics. 2014;**2**(2):143-151

[45] Hejny RW, Lorenz RD. Evaluating the practical low-speed limits for back-EMF tracking-based sensorless speed control using drive stiffness as a key metric. IEEE Transactions on Industry Applications. 2011;**47**(3):1337-1343

[46] Sarikhani A, Mohammed OA. Sensorless control of PM synchronous machines by physics-based EMF observer. IEEE Transactions on Energy Conversion. 2012;**27**(4):1009-1017

[47] Antonello R, Ortombina L, Tinazzi F, Zigliotto M. Enhanced low-speed operations for sensorless anisotropic PM synchronous motor drives by a modified back-EMF observer. IEEE Transactions on Industrial Electronics. 2018;**65**(4): 3069-3076

[48] Hideaki I, Masanobu I, Takeshi K Kozo I. Hybrid sensorless control of IPMSM for direct drive applications. In:

Proceedings of IEEE IPEC; 2010.
pp. 2761-2767

[49] Lara J, Chandra A, Xu J. Integration of HFSI and extended-EMF based techniques for PMSM sensorless control in HEV/EV applications. In: 2012 Annual Conference on IEEE Industrial Electronics Society (IECON); 2012. pp. 3688-3693

[50] Lipo TA. Synchronous reluctance machine—A viable alternative for AC drive. Electric Machine & Power System. 1991;**19**(6):659-671

[51] Matsuo T, Lipo TA. Rotor design optimization of synchronous reluctance machine. IEEE Transactions on Energy Conversion. 1994;**9**(2):359-365

[52] Bianchi N, Bolognani S, Carraro E, Castiello M, Fornasiero E. Electric vehicle traction based on synchronous reluctance motors. IEEE Transactions on Industry Applications. 2016;**52**(6): 4762-4769

[53] Qu Z, Hinkkanen M. Loss-minimizing control of synchronous reluctance motors—A review. Proceedings of IEEE ICIT; 2013. pp. 350-355

[54] Lubin T, Razik H, Rezzoug A. Magnetic saturation effects on the control of a synchronous reluctance machine. IEEE Transactions on Energy Conversion. 2002;**17**(3):356-362

[55] Hofmann HF, Sanders SR, EL-Antably A. Stator-flux-oriented vector control of synchronous reluctance machines with maximized efficiency. IEEE Transactions on Industrial Electronics. 2004;**51**(5):1066-1072

[56] Zarchi HA, Soltani J, Markadeh GRA, Fazeli M, Sichani AK. Variable structure direct torque control of encoderless synchronous reluctance motor drives with maximized efficiency. In: Proceedings of IEEE ISIE; 2010. pp. 1529-1535

[57] Kim S, Sul SK, Ide K, Morimoto S. Maximum efficiency operation of synchronous reluctance machine using signal injection. In: Proceedings of IEEE ECCE; 2010. pp. 2000-2004

[58] Inoue Y, Morimoto S, Sanada M. A novel control scheme for maximum power operation of synchronous reluctance motors including maximum torque per flux control. IEEE Transactions on Industry Applications. 2011;**47**(1):115-121

[59] Yamamoto S, Hirahara H, Adawey JB, Ara T, Matsuse K. Maximum efficiency drives of synchronous reluctance motors by a novel loss minimization controller with inductance estimator. IEEE Transactions on Industry Applications. 2013;**49**(6):2543-2551

[60] Varatharajan A, Cruz S, Hadla H, Briz F. Predictive torque control of SynRM drives with online MTPA trajectory tracking and inductances estimation. In: Proceedings of IEEE IEMDC; 2017. pp. 1-7

[61] Bedetti N, Calligaro S, Petrella R. Self-adaptation of MTPA tracking controller for IPMSM and SynRM drives based on on-line estimation of loop gain. In: Proceedings of IEEE ECCE; 2017. pp. 1917-1924

[62] Mahmoud H, Bianchi N. Nonlinear analytical model of eccentric synchronous reluctance machines considering the iron saturation and slotting effect. IEEE Transactions on Industry Applications. 2017;**53**(3):2007-2015

[63] Wang KC. A battery/supercapacitor powered EV PMSM drive with grid connected and energy harvesting functions [thesis]. Hsinchu, ROC: Department of Electrical Engineering, National Tsing Hua University; 2017

[64] Su SW. Development of a synchronous reluctance motor drive and

its position sensorless control study
[thesis]. Hsinchu, ROC: Department of
Electrical Engineering, National Tsing
Hua University; 2017

[65] Zhuang JX, Development of
position sensorless synchronous-
reluctance generator system and its
performance enhancement controls
[thesis]. Hsinchu, ROC: Department of
Electrical Engineering, National Tsing
Hua University; 2018